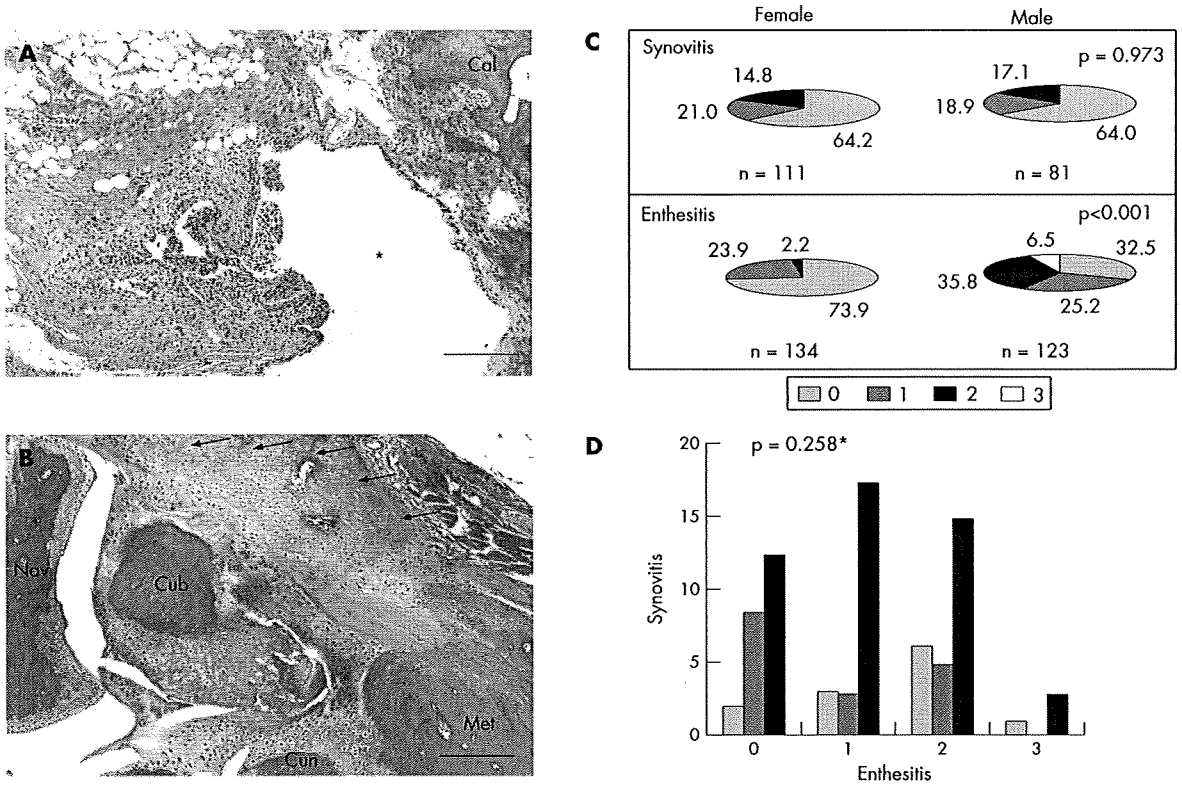

Figure 1 Specific manifestations of the synovitis or enthesitis developed in MCF_2 mice. Representative microscopic manifestations of synovitis (A) and enthesitis (B) in aged MCF_2 mice. Asterisk in (A) indicates a synovial cavity; arrows in (B) indicate the entheseal proliferation of ankle-associated tendon sheath (haematoxylin and eosin). Bars indicate 200 μm. (C) Percentage distribution of grades of synovitis and enthesitis in aged MCF_2 mice. The number of the mice analysed and p values provided by the χ^2 test are indicated. (D) The bar graph indicates the number distribution of grades of enthesitis and synovitis in the 81 male MCF_2 mice. No correlation is shown between the onsets of synovitis and enthesitis. p Value was determined by Fisher's exact test with standard 3×4 contingency matrices. Cub, cuboidal bone; Met, metatarsal bone; Nav, navicular bone; Cal, calcaneus; Cun, cuneiform bone.

proliferation (grade 2). The grade of an individual mouse was defined as a maximal grade determined in six longitudinal sections of bilateral hind paws. Samples inappropriate for microscopical examination, mainly because of the absence of synovium in accountable sections, were precluded from further analysis. The number of female and male MCF_2 mice accounted in this study was 111 and 81, respectively. The grade of ankylosis was determined previously.[5]

Genomewide screening for susceptibility loci to synovial proliferation

We searched association loci in the whole genome using 81 male MCF_2 mice and 73 microsatellite markers, which were all able to distinguish the parental genotypes and provided a coverage of the mouse genome with an average distance of 23.3 cM apart. The genetic positions of microsatellite markers and genes were determined on the basis of the Mouse Genome Informatics provided by The Jackson Laboratory.

Statistical analysis

A correlation between the grades of synovial proliferation and ankylosis was evaluated by Fisher's exact test with standard 3×4 contingency matrices. An association of the onset of synovial proliferation and the genotype at each marker position was evaluated by the χ^2 test with standard 2×3 contingency matrices. A significant or suggestive association was estimated by $p<0.000052$ or 0.0016, respectively, as recommended by Lander and Kruglyak.[7]

Table 1 Association of microsatellite genotype and the incidence of synovitis in MCF_2 male mice

		Incidence of synovitis							
	Position	Negative			Positive				
Marker	(CM)	*MM*	*MC*	*CC*	*MM*	*MC*	*CC*	χ^2 test	p Value
D11Mit71	1.1	13	25	14	7	16	6	0.48	0.79
D11Mit263	55.6	9	32	11	17	8	4	14.8	0.001
D11Mit334	68	11	29	12	12	13	4	3.92	0.14
D11Mit338	75	10	30	12	11	12	6	3.51	0.17

Genotypes *MM*, *MC* and *CC* indicate MRL/MRL homozygote, MRL/C3H heterozygote and C3H/C3H homozygote, respectively.

RESULTS

Incidence of synovial proliferation

In addition to the onset of ankylosis, we observed a thickening of the synovial lining layer, with mild lymphocytic infiltration and proliferation of small vessels in MCF_2 mice (fig 1A,B). Villous formations were evident in the advanced stage of the synovial proliferation. Neither lymphoid aggregation in the synovial lesion nor bone erosion with pannus-like formation was detected in all the mice examined. The microscopical incidence of synovial proliferation was 12/25 (48%) in MRL/rpl, 12/26 (46.2%) in C3H/lpr, 14/69 (20.3%) in MCF_1 and 69/192 (35.9%) in MCF_2 mice. The synovial lesion was detected equally in male and female MCF_2 mice ($p = 0.973$) (fig 1C). No significant correlation was obtained between the progression of ankylosis and synovial proliferation in male-only ($p = 0.258$, fig 1D) and all MCF_2 mice (data not shown).

Mapping of susceptibility loci associated with synovial proliferation

In this mapping study, we analysed the same MCF_2 mice that were used in the previous mapping study on ankylosis. The genomewide search using 81 male mice suggested a single marker *D11Mit263* (55.6 cM) on chromosome 11 that was significantly associated with the onset of synovial proliferation ($p<0.001$; table 1). The incidence of synovial proliferation in the MRL homozygote group (17/26, 65.4%) in association with *D11Mit263* was higher than that in the MRL/C3H heterozygote (8/40, 20%) and C3H homozygote (4/15, 26.7%) groups. This indicates that this MRL-derived locus regulates the onset of synovial proliferation in a recessive inheritance manner. No significant association was observed between synovial proliferation and any marker on the X chromosome where the SAP gene exists.

DISCUSSION

Recent studies have reported several mouse models with spontaneous ankylosis. DBA/1 is a spontaneous ankylosis model and an induced synovitis model with immunisation of type II collagen. The two DBA/1-related arthopathies develop similarly in a male-predominant fashion, although they are histopathologically different. It has been of particular interest to determine whether the pathogenic mechanisms of the distinct arthropathies in the DBA/1 mice are overlapped.

A cross mating of the DBA/1 strain with a particular lupus-prone strain such as BXSB or MRL/Mp resulted in an acceleration of the onset and increase in the severity of ankylosis in F_1 mice.[2 4] These facts may suggest a correlation between lupus susceptibility and the pathogenesis of ankylosis. The MCF_2 mice used in this study also shared lupus-prone and synovitis-prone genetic backgrounds with MRL/lpr mice to varied extents. Previous studies have shown some MRL alleles significantly linked to the onset of spontaneous synovitis in the *lpr* constraint.[8 9] Therefore, there is a reason for the onset of synovitis in MCF_2 mice. This study showed the onset of synovitis in MCF_2 mice, although inflammation and erosive changes were present to a lesser extent than those in the original MRL/lpr mice. We thought that this was a countereffect of ankylosis on synovitis; however, this notion turned out to be erroneous. This may be partly due to the difference in bleeding condition and genetic effects derived from the C3H/lpr strain. Our results totally revised these considerations and enforced a notion that proliferating enthesitis entail specific mechanisms for the development of ankylosis.

Our results suggest a susceptibility locus in the middle of chromosome 11. As the number of markers and samples were not sufficient to detect complex loci, some loci may have remained undetected. However, the detected locus has a major effect on the development of synovial proliferation. This locus contains several genes that are highly conserved in a particular interval of human chromosome 17. To date, a high-resolution linkage and association mapping study identified a susceptibility locus for rheumatoid arthritis in this region.[10] The central part of mouse chromosome 11 also contains several loci associated with experimental autoimmune encephalomyelitis,[11 12] collagen-induced arthritis[13] and proteoglycan-induced arthritis.[14] This region is noteworthy when considering the genetic predisposition of rheumatoid arthritis.

A previous study using a larger number of backcross mice prepared from the same parental strains of MRL/Mp and C3H/He indicated that the five linkage loci are associated with the onset of arthritis.[9] None of these loci overlap with the present linkage region. This discrepancy is possibly due to a difference in the mouse generation used (N_2 or F_2), a difference in the housing condition or a suppressive effect of the Y chromosome derived from C3H/lpr as discussed previously while purporting a possible reason for the onset of new cases of ankylosis.[5]

ACKNOWLEDGEMENTS

We thank Ms N Yamaki, Dr N Tanda and Dr H Umeda for technical assistance, Mrs N Fujisawa for secretarial assistance and Dr M Nose for critical comments.

Authors' affiliations

Ming-Cai Zhang*, Fumiko Date, Hiroshi Furukawa, Masao Ono, Department of Pathology, Tohoku University Graduate School of Medicine, Sendai, Miyagi, Japan
Shiro Mori*, Department of Oral Medicine and Surgery, Tohoku University Graduate School of Dentistry, Sendai, Miyagi, Japan

*These authors contributed equally to this work.

Funding: This study was supported by Grants-in-Aid for Scientific Research from the Ministry of Education, Science, Sports, and Culture of Japan to SM (number 15390607) and MO (number 16390113).

Competing interests: None.

Correspondence to: Dr Masao Ono, Department of Pathology, Tohoku University Graduate School of Medicine, 2-1 Seiryo, Aoba, Sendai, Miyagi 980-8575, Japan; onomasao@mail.tains.tohoku.ac.jp

Accepted 10 July 2006
Published Online First 25 July 2006

REFERENCES

1 **Nordling C**, Karlsson-Parra A, Jansson L, Holmdahl R, Klareskog L. Characterization of a spontaneously occurring arthritis in male DBA/1 mice. *Arthritis Rheum* 1992;**35**:717–22.
2 **Holmdahl R**, Jansson L, Andersson M, Jonsson R. Genetic, hormonal and behavioural influence on spontaneously developing arthritis in normal mice. *Clin Exp Immunol* 1992;**88**:467–72.
3 **Lories RJ**, Matthys P, de Vlam K, Derese I, Luyten FP. Ankylosing enthesitis, dactylitis, and onychoperiostitis in male DBA/1 mice: a model of psoriatic arthritis. *Ann Rheum Dis* 2004;**63**:595–8.
4 **Oishi H**, Miyazaki T, Mizuki S, Kamogawa J, Lu LM, Tsubaki T, *et al*. Accelerating effect of an MRL gene locus on the severity and onset of arthropathy in DBA/1 mice. *Arthritis Rheum* 2005;**52**:959–66.
5 **Mori S**, Zhang MC, Tanda N, Date F, Nose M, Furukawa H, *et al*. Genetic characterization of spontaneous ankylosing arthropathy with unique inheritance from Fas-deficient strains of mice. *Ann Rheum Dis* 2006;**28**:1273–8.
6 **Komori H**, Furukawa H, Mori S, Ito MR, Terada M, Zhang MC, *et al*. A signal adaptor SLAM-associated protein regulates spontaneous autoimmunity and Fas-dependent lymphoproliferation in MRL-*Fas*^{lpr} lupus mice. *J Immunol* 2006;**176**:395–400.
7 **Lander E**, Kruglyak L. Genetic dissection of complex traits: guidelines for interpreting and reporting linkage results. *Nat Genet* 1995;**11**:241–7.
8 **Hang L**, Theofilopoulos AN, Dixon FJ. A spontaneous rheumatoid arthritis-like disease in MRL/l mice. *J Exp Med* 1982;**155**:1690–701.
9 **Kamogawa J**, Terada M, Mizuki S, Nishihara M, Yamamoto H, Mori S, *et al*. Arthritis in MRL/lpr mice is under the control of multiple gene loci with an allelic combination derived from the original inbred strains. *Arthritis Rheum* 2002;**46**:1067–74.
10 **Barton A**, Eyre S, Myerscough A, Brintnell B, Ward D, Ollier WE, *et al*. High resolution linkage and association mapping identifies a novel rheumatoid

arthritis susceptibility locus homologous to one linked to two rat models of inflammatory arthritis. *Hum Mol Genet* 2001;**10**:1901–6.
11 **Karlsson J**, Zhao X, Lonskaya I, Neptin M, Holmdahl R, Andersson A. Novel quantitative trait loci controlling development of experimental autoimmune encephalomyelitis and proportion of lymphocyte subpopulations. *J Immunol* 2003;**170**:1019–26.
12 **Butterfield RJ**, Blankenhorn EP, Roper RJ, Zachary JF, Doerge RW, Teuscher C. Identification of genetic loci controlling the characteristics and severity of brain and spinal cord lesions in experimental allergic encephalomyelitis. *Am J Pathol* 2000;**157**:637–45.
13 **Liljander M**, Sallstrom MA, Andersson S, Andersson A, Holmdahl R, Mattsson R. Identification of collagen-induced arthritis loci in aged multiparous female mice. *Arthritis Res Ther* 2006;**8**:R45.
14 **Adarichev VA**, Nesterovitch AB, Bardos T, Biesczat D, Chandrasekaran R, Vermes C, *et al*. Sex effect on clinical and immunologic quantitative trait loci in a murine model of rheumatoid arthritis. *Arthritis Rheum* 2003;**48**:1708–20.

APMIS 115: 1350–6, 2007
Printed in Denmark . All rights reserved

ISSN 0903-4641

Persistent expression of an unproductive immunoglobulin heavy chain allele with D_H-J_H-γ configuration in peripheral tissues

MASAO ONO[1] and MASATO NOSE[2]

[1]Department of Pathology, Tohoku University Graduate School of Medicine, Sendai, and [2]Department of Pathology, Ehime University School of Medicine, Toon, Japan

Ono M, Nose M. Persistent expression of an unproductive immunoglobulin heavy chain allele with D_H-J_H-γ configuration in peripheral tissues. APMIS 2007;115:1350–6.

Genomic recombination events, including VDJ recombination (VDJR) and class-switch recombination (CSR), are indispensable for the adaptation and progression of the acquired immune system. These processes are completed by orderly, temporal onsets of the gene rearrangements along with B-cell differentiation. The presence of various premature transcripts of immunoglobulin heavy chain (IgH) alleles has been demonstrated during B-cell ontogeny. These include D_H-J_H (DJ)-μ, J_H-μ, and sterile transcripts of C_H. Since these transcripts can be detected during the onset of VDJR and CSR, their presence is believed to reflect a structural change in the genome, favoring VDJR and CSR. This report presents evidence of persistent DJ transcription and onset of CSR on an unproductive IgH allele in peripheral tissues. Nucleotide sequence analysis revealed that these transcripts showed DJ-γ (Dγ) configuration and that characteristics of the variable region were essentially the same as those of the DJ-μ transcript previously described. It was noted that the small intestine abundantly expresses Dγ transcripts with γ2b and γ1 isotypes of the IgH constant region. The present findings indicate the onset of CSR preceding V_H to DJ joining in an unproductive IgH allele of the peripheral B cell and the specificity for the gut-associated condition for B-cell differentiation in the small intestine.

Key words: B cell; immunoglobulin; class switching; VDJ rearrangement; DJ transcript.

Masao Ono, Department of Pathology, Tohoku University Graduate School of Medicine, 2-1 Seiryo, Aoba-ku, Sendai, Miyagi 980-8575, Japan. e-mail: onomasao@mail.tains.tohoku.ac.jp

An immunoglobulin (Ig) heavy chain (IgH) gene consists of heterogeneous gene segments that separately code the four parts of IgH protein: the variable segment (V_H), diversity segment (D_H), junction segment (J_H), and constant region (C_H). Assemblies of V_H, D_H, and J_H segments, referred to as VDJ recombination (VDJR), necessarily occur during B-cell development in bone marrow and consequently form a continuous coding exon for the IgH-variable region (1). VDJR is an essential process for the acquisition of a broad range of structural variations of IgH that enable adaptive immune recognition of various pathogens. With the progression of the immune response, a subsequent process known as class-switch recombination (CSR) occurs in peripheral tissues (2–5) and changes an isotype of C_H, resulting in alteration of the effector functions of Ig. Disorders associated with defective CSR usually cause immune insufficiency in humans and mice (6–12); therefore, CSR is indispensable for normal development of the humoral immune response.

IgH gene alleles express germ line transcripts during B-cell differentiation, including JH-μ

Received 12 June 2007.
Accepted 2 July 2007.

(13), D_H-J_H (DJ)-μ (Dμ) (14) and sterile C_H transcripts (15–19). Although none of these transcripts exerts an effector function as an antibody, these are detected before or during the onset of VDJR and CSR in B-lineage cells. It has been proposed that these sterile transcripts participate in the formation of the structure of the IgH gene accessible for the factors involved in VDJR and CSR as well as the transcriptional regulators for these transcriptions.

We had previously searched for the nucleotide sequences of IgH transcripts of mouse hybridoma clones isolated from MRL/lpr, which was an autoimmune-prone strain of mice due to the defect in the apoptosis receptor gene—Fas (20, 21). In this study we identified an aberrant IgH transcript that represented a truncated variable region—DJ—with γ3 isotype of C_H (unpublished data). This finding suggested the presence of the DJ-γ (Dγ) transcript in the spleen of an MRL/lpr strain. Here we tested whether this aberrant transcript was expressed in peripheral tissues and in an autoimmune-dependent and/or a Fas-dependent fashion. The results provide the first evidence for the persistent expression of Dγ transcripts in mouse peripheral tissues. The present findings showed the fate of unproductive IgH alleles in peripheral environments and characteristics of IgH alleles associated with a specific immunological nature of the small intestine.

MATERIALS AND METHODS

Mice

MRL/Mp.*Fas*^{lpr} (MRL/lpr), C57BL/6.*Fas*^{lpr} (B6/lpr), and MRL/MpJ (MRL/+) strains of mice were obtained from the Jackson Laboratory (Bar Harbor, ME). C.B-17/Icr-scid/scid (SCID) mice were kindly donated by Dr. S. Ikehara (Kansai Medical University, Osaka, Japan). All mice were bred under specific pathogen-free conditions at the Institute for Animal Experimentation, Tohoku University, Sendai, Japan. The Tohoku University guidelines for animal experimentation were observed.

RNA preparation and analysis

Total RNA was prepared from thymus, spleen, axillary lymph nodes, mesenteric lymph node, peritoneal resident cells, small intestine with Peyer's patches, and bone marrow cells according to the regular protocol for Trisol™ agent (Invitrogen, Carlsbad, CA). Total RNA (20 μg) was denatured, electrophoresed in 1.2% agarose gel, and transferred onto a nylon membrane (BioRad, Tokyo, Japan) by the capillary transfer method. A hybridization probe (D_{SP2} probe, 78 nucleotide length) for the detection of DJ transcripts was prepared from a cloned cDNA containing the 5′-flanking sequence of the $D_{SP2.2}$ gene in pBluescript KS+ vector, which was obtained from the hybridoma 8H8 clone by reverse transcription-polymerase chain reaction (RT-PCR) with $D_{SP2.2}$ specific primers: D_{SP2}F1, 5′-ACTCTGCACTGCTACCTCTGG-3′, and D_{SP2}R1, 5′-GACAAAAATCCCTGCCAAGTAAGG-3′ (Fig. 1). It is known that the sequence of this amplified region is highly conserved among all members of the D_{SP2} family. Radioisotope labeling with [α^{32}P] dCTP was achieved by DNA polymerase reaction in the presence of the $D_{SP2.2}$ specific primers and 25 ng of the probe DNA. Hybridizations and washes were performed as described previously (22). The washed membrane was exposed to a high-sensitive film (Kodac X-OMAT AR) for 2 weeks.

RT-PCR and identification of the IgG subclass

Single-strand cDNA was prepared from 2 μg of total RNA with oligo-dT primers (50 pmol) and reverse transcriptase (200 U) derived from Moloney murine leukemia virus (Invitrogen). In RT-PCR, $V_{H\ BACK}$, AGGT[C,G][C,A]A[G,A]CTGCAG[C,G]AGTC[T,A]GG (23), or D_{SP2}F2, TTACTTGGCAGGGATTTTTG, and [^{32}P] 5′-end-labeled Cγ32, 5′-TGCATTTGAACTCCTTGCC-3′, which is commonly present in all mouse IgG subclasses, were used to amplify V_H-D_H-J_H (VDJ)-γ or Dγ transcripts, respectively. The sequences of $V_{H\ BACK}$ and D_{SP2}F2 are known to be commonly present in the $V_{H\ J558}$ family genes and D_{SP2} family genes, respectively. The expression profile of IgG subclasses was determined by RT-PCR followed by digestions with *Bam* HI and *Xba* I endonucleases (22) (Fig. 3A).

Nucleotide sequencing

The RT-PCR products amplified with D_{SP2}F2 and Cγ32 (non RI-labeled) were phosphorylated by nucleotide kinase reaction and cloned into a pBluescript

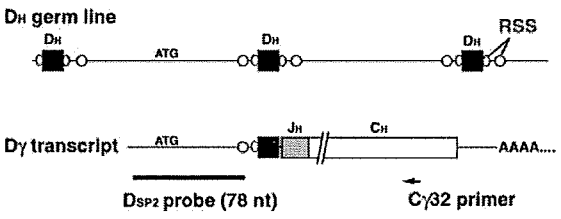

Fig. 1. Hybridization probe to detect DJ transcripts in Northern hybidization analysis. The probe fragment corresponds to the 5' flanking sequence of the $D_{SP2.2}$ gene. *RSS*, recombination signal sequence; D_H, a coding segment for the diversity segment of IgH; ATG, initiation codon; nt, nucleotide length.

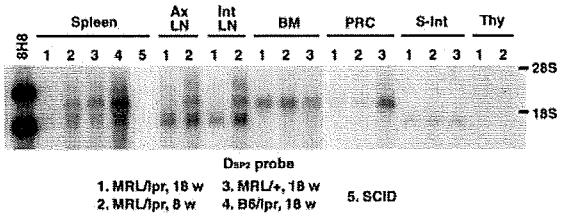

Fig. 2. Expression of DJ transcripts *in vivo*. Total RNA samples (20 μg/lane) prepared from indicated various organs or a cell type were analyzed with Northern hybridization using the ^{32}P-labeled D_{SP2} probe as shown in Fig. 1. The lower molecular weight signal of 8H8 corresponds to the Dγ3 transcript. *Ax LN*, axillary lymph node; *Int LN*, intestinal lymph node; *BM*, bone marrow; *PRC*, peritoneal resident cells; *S-Int*, small intestine; *Thy*, thymus; *18S*, ribosomal RNA 18 S; *28S*, ribosomal RNA 28S; SCID, severe combined immunodeficiency strain of mice.

KS+ vector. Nucleotide sequences in randomly selected clones were determined by dideoxy termination reactions.

RESULTS

Expression of DJ transcripts in peripheral tissues

We performed Northern hybridization with the D_{SP2} probe (Fig. 1) to show the presence of premature IgH transcripts containing the 5′ flanking sequence of the D_{SP2} family genes and, if present, their specificity to the autoimmune onset in MRL/lpr mice. Total RNA samples were prepared from various immune tissues of mice, including 8- and 18-week-old mice, as controls of pre-diseased and diseased conditions, respectively (Fig. 2). It was of particular note that specific signals appeared in heterogeneous and tissue-specific patterns. The spleen, axillary lymph node, and mesenteric lymph node expressed at least three different transcripts. In comparison, the bone marrow, peritoneal resident cells, and small intestine showed simpler patterns; the bone marrow and peritoneal resident cells expressed longer transcripts, while the small intestine expressed shorter transcripts. No signal was detected in the spleen of SCID mice, which lack both B and T cells due to the genetic defect in VDJR. This finding indicates high specificity of the D_{SP2} probe in detection of the transcripts containing the 5′ flanking region of the D_{SP2} family genes.

A previously isolated hybridoma clone, namely 8H8, was also analyzed as a reference for the Dγ transcript in this study. This hybridoma clone was established from the spleen of an autoimmune-prone strain MRL/lpr. A sequencing analysis of 8H8 revealed the expression of an aberrant transcript with Dγ configuration that contained the 5′ flanking region of the $D_{SP2.2}$ gene segment (data not shown). These findings had suggested that the *lpr* mutation, which is known to cause the defect in the apoptosis-related receptor Fas and the onset of autoimmune diseases, also caused the pathological expression of such aberrant transcripts. Our present findings did not support this possibility because no distinct signal was observed for the MRL/lpr preparations.

Identification and characterization of IgG-class-switched DJ transcripts

The presence of the longer transcripts was demonstrated in various immune tissues as well as the bone marrow except the small intestine (Fig. 2). It seemed reasonable to consider that the longer transcripts were Dμ because past studies had shown the presence of Dμ in the bone marrow. On the other hand, the shorter transcripts remained to be elucidated. A further suggestion respecting this issue arose from the demonstration of shorter transcripts in 8H8, which is a mouse hybridoma shown to express a Dγ transcript. Therefore, we attempted to amplify Dγ transcripts in the spleen and small intestine by RT-PCR. Using the consensus primers D_{SP2}F2 and Cγ32 (Fig. 3A), we obtained the amplification for cDNA prepared from the spleen and small intestine, and succeeded in cloning them in plasmid vectors. 100 clones were randomly isolated for each tissue and analyzed further. Of these, 38 spleen-derived and 18 small intestine-derived clones were found to harbor insert fragments with a Dγ configuration. Excluding repeatedly appearing clones recognized by sequence identity, 17 spleen-derived and 9 small intestine-derived clones were finally obtained as independent clones. Their sequence data demonstrated that the Dγ transcript in the spleen shared common characteristics with the Dμ transcript or DJ genomic fragment reported previously (23–26): under-representation of RF2 in the D_H segment (Dμ selection), presence of D_H-D_H joining, usage of $D_{H\ SP2.12}$ and $D_{H\ SP2.13}$ previously iden-

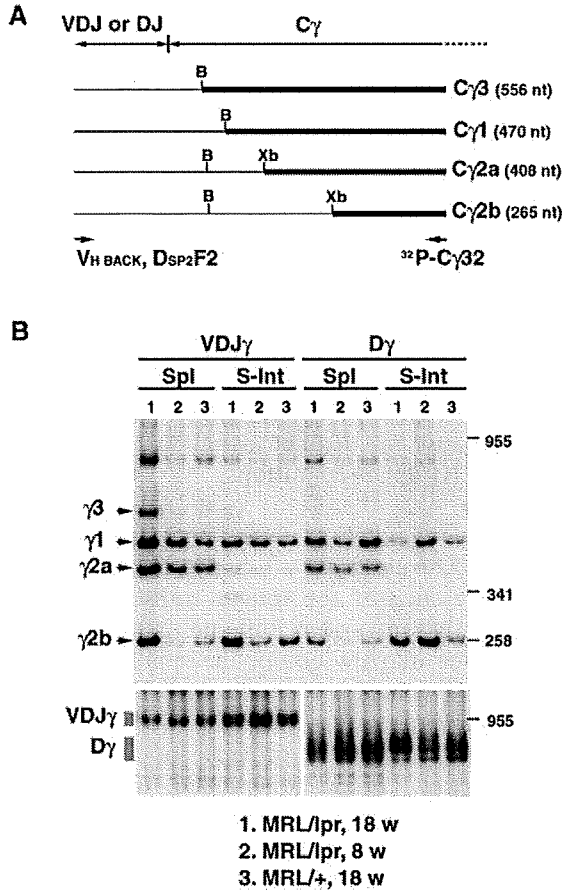

Fig. 3. Expression profile of IgG isotypes in the spleen and small intestine in MRL strains of mice. (A) Schematic representation of the differential detection of four IgG subclasses at an mRNA level. $V_{H\,BACK}$ or $D_{SP2}F2$ primer was used for the amplification of VDJ-γ or Dγ transcript, respectively. (B) *BamHI*; *Xb*, *XbaI*. *B*, IgG isotype profile of VDJ-γ and Dγ transcripts in the spleen and small intestine. A signal corresponding to each IgG isotype was indicated. Cγ; IgG constant region; Cγ3, IgG3 constant region; Cγ1, IgG1 constant region; Cγ2a, IgG2a constant region; Cγ2b, IgG2b constant region; *Spl*, spleen; *S-Int*, small intestine; nt, nucleotide length.

tified in MRL/lpr, and frequent N nucleotide insertions in the spleen of aged mice (Table 1). These characteristics were found to be largely true for the small intestine; however, lower frequencies of N insertions and RF1 usage in the small intestine than in the spleen are not precluded.

An isotype pattern of Dγ constant region was explored by the semi-quantitative method developed previously (22) (Fig. 3A). The results demonstrated a tissue- and age-specific isotype pattern of Dγ and VDJ-γ transcripts (Fig. 3B). Dγ and VDJ-γ transcripts in the small intestine represented a remarkable predominance of γ1 and γ2b isotypes in all mice examined. An aging-dependent relative increase in the expression of γ2b and γ3 of VDJ-γ and γ2b of Dγ was observed in the spleen of the MRL/lpr strain.

DISCUSSION

The present study provided the first evidence of the presence of Dγ transcripts in peripheral tissues. D_H to J_H joining followed by Dμ transcription readily takes place on both IgH alleles of a pro-B cell in the bone marrow. The subsequent joining, V_H to DJ, followed by activation of the V_H promoter on either allele achieves transcription for the production of the IgM heavy chain in the bone marrow, while, in a case where the transcription is productive for IgM, the other allele is no longer processed. This abortive allele is so far considered to be the origin of all DJ transcripts in the peripheral tissues.

Northern hybridization revealed that different kinds of DJ transcripts are present in the peripheral tissues. The expression level of these DJ transcripts seems to be so low that it has taken 2 weeks for the specific signal of the hybridized probe to be visible. However, the level of their peripheral expression is comparable to the bone marrow. Provided that bone marrow mainly produces Dμ transcripts, spleen, lymph node, thymus, and small intestine produce other types of DJ transcripts than Dμ. The present sequence data and RT-PCR-based isotyping data confirmed the presence of Dγ transcripts in the spleen and small intestine, indicating that the transcription and the onset of CSR occur on unproductive IgH alleles in peripheral tissues. Although the biological significance of the peripheral expression of DJ transcripts remains unclear, these findings provide new insights into tissue specificity in peripheral B-cell differentiation or the mechanism for B- cell receptor editing in peripheral tissues.

Dμ transcripts harbor a leader peptide sequence in the 5′-region. Therefore, Dμ transcripts with a particular reading frame—RF2—can be translated into a cell surface protein con-

TABLE 1. *Characteristics of Dγ transcripts in the spleen and small intestine of an MRL/lpr mouse*[1)]

Clone ID	DH sequence	N/P sequence	JH sequence	J_H[2)]	C_H	D_H[3)]
I. Spleen						
S16	TC TAC TAT GGT GAC TAC	GGC GGA	TTT GCT TAC TGG	3	γ2a	2.13
S17–1	CC TAC TAT AGT AAC TAC	GTG GG	T GCT ATG GAC TAC TGG	4	γ3	2.x
S17–2	CC TAC TAT AGT AAC TAC TTA CGA	GGG ATT	TTT GCT TAC TGG	3	γ3	2.x+2.2
S36	CC TAC TAT AGT AAC TAC	GTT TG	T GCT ATG GAC TAC TGG	4	γ1	2.x
S39	CC TAC TAT AGT TAC TAT AGT TAC G		CC TGG TTT GCT TAC TGG	3	γ2a	2.12
S65	CC TAC TAT AGT AAC T		GG TTT GCT TAC TGG	3	γ1	2.x
S70	CC TAC TAT AGT TAC T		CC TGG TTT GCT TAC TGG	3	γ1	2.12
S9	CC TA	A GG	T GCT ATG GAC TAC TGG	4	γ2a	2.10,12, or x
S77	TCT ATG ATG GTT ACT A	AA CC	C TGG any	γ1	2.9	
S8	CCT ACT ATA GTT ACT ATA GTT ACG AC	G T	AC TAC TTT GAC TAC TGG	2	γ2b	2.12
S11	C CTA CTA TAG TAA CT	T TCT	TTT GCT TAC TGG	3	γ2b	2.x
S33	C CTA CTA TAG TTA CTA TAG TTA CG	G AAC TCC T	AT TAC TAT GCT ATG GAC TAC TGG	4	γ2b	2.12
S37[5)]	C CTA CTA TAG TAA C	CG AGG	GCT TAC TGG	3	γ1	2.x
S38	T CTA CTA TGG TGA CT	T TTT	TAT GCT ATG GAC TAC TGG	4	γ3	2.13
S43	C CTA CTA TAG TAA C	CG AGG	GCT TAC TGG	3	γ2a	2.x
S63	T CTA CTA	CCC A	AC TGG any	γ2b	2.2, 5, or 13	
S7	C CTA CTA TAG TTA	GGG CGT	TTT GCT TAC TGG	3	γ2a	2.12
II. Small intestine						
I27	CCT ACT ATA GTA ACT AC	G TGA TGA	GAC TAC TGG	2 or 4	γ2b	2.x+2.9
I22	C CTA CTA TAC	GTA CGA	TTT GAC TAC TGG	2	γ2b	2.x+2.10
I28	C CAA CTA TAG TAA	TTT TT	C TAT GTT ATG GAC TAC TGG	4	γ2b	2.x
I32	C CTA CTA TA		T GTT ATG GAC TAC TGG	4	γ2b	2.x, 10, or 12
I51	C CTA CTA TAG TA		C TAT GTT ATG GAC TAC TGG	4	γ2b	2.x
I57[6)]	C CTA CTA		GGG TTT TCT TAC TGG	3	γ1	2.x, 10, or 12
I71	C CTA CTA		GGG TTT TCT TAC TGG	3	γ2b	2.x, 10, or 12
I74	T CTA TGA TGG TTA CTA C		AT GTT ATG GAC TAC TGG	4	γ2b	2.9
I75	C CTA CTA TAG TAA C	CT CGG AGG	GTT ATG GAC TAC TGG	4	γ2b	2.x

[1)] We used cDNA derived from a 20-week-old male MRL/lpr mouse for this sequence analysis. A residue of mutation is underlined.
[2)] A JH family designation was determined according to the genomic sequence of C57BL/6 in the public data base.
[3)] A DH SP2 family designation was determined according to the genomic sequences in the public data base (Accession number: J00431, J00432, J00433, J00435, J00437, J00438 or in previous reports (Kaartinen & Mekela, 1985, Feeney, 1990, Gu et al., 1991, Kompfner et al., 2001).
[4)] A RF was determined by the numbering system proposed in a previous report.
[5)] S37 is a γ isotype-switching variant of S43.
[6)] I57 is a γ isotype-switching variant of I71.

taining an IgM constant region (14). Although the rationale underlying the expression of the Dμ protein is not completely elucidated, it has been shown that the RF2 usage in Dμ transcripts is under-represented in B-lineage cells but not in T-lineage cells, which, however, in part, undergo DJ joining in conjunction with T-cell receptor (TCR) rearrangement (24). It is proposed that the Dμ protein physiologically mediates signals for the elimination of pro-B cells in the bone marrow. The present study has shown the under-representation of RF2 usage for Dγ transcripts in the spleen and small intestine, as previously demonstrated for Dμ transcripts in the bone marrow. This finding indicates that the cells producing Dγ transcripts in the peripheral tissues have undergone Dμ selection in the bone marrow; therefore, they are B-lineage cells. The frequent usage of RF3 was noted for the Dγ transcripts in the small intestine. This should be confirmed by further sequence analyses.

The findings on VDJ-γ and Dγ isotype pattern of IgG constant regions clearly indicate selective expression of γ2b and, to a lesser extent, γ1 of C_H in the small intestine. The different isotype pattern was observed in the spleen in the same individual (Fig. 3B). This may suggest that the tissue-specific environment controls the onset of CSR in peripheral B cells. Intestinal mucosa is known to present a specific condition for B cells that favors CSR to α isotype of C_H (27–29). Transforming growth factor-β (TGF-β) has been shown to deliver a gut-associated signal through TGF-β receptor 2 (30). Past studies have shown that TGF-β facilitates CSR to IgG2b as well as IgA at the culture level (31, 32). The over-representation of IgG2b subclass in the small intestine may be associated with the gut-associated condition. In addition, it is noted that both productive and unproductive alleles of IgH present a similar isotype pattern in the spleen and small intestine. This sug-

gests that the two IgH alleles are under the same regulation for CSR.

Our preliminary finding from a 8H8 hybridoma clone isolated from an autoimmune-prone strain of mice—MRL/lpr—provides insight into the association of Dγ transcripts with an autoimmune mechanism. The present study has shown that the Dγ transcripts derived from MRL/lpr do not represent a specific pattern in the IgH isotype distribution in the spleen and small intestine. The nucleotide sequence data confirmed that the forbidden RF usage in Dμ transcript in bone marrow—RF2—was not activated in association with the autoimmune onset in aged MRL/lpr, further suggesting that Fas is not involved in the elimination of RF2 usage in B cells in peripheral tissues. The relative increase of γ3 isotype in the spleen of aged MRL/lpr was also noted in the present study. This confirms our previous finding of high expression of IgG3 in aged MRL/lpr (33). IgG3 is specifically induced in mice by bacterial antigens, i.e., lipopolysaccharide, and has long been considered the disease-associated antibody subclass in this strain. Small intestine has been thought to be a responsible organ where IgG3 is produced in response to antigens of commensal bacteria in this strain; however, the present results confute this idea. The role of Dγ transcription in physiological and pathological B-cell development remains to be elucidated.

The authors thank Tokuo Yamamoto for critical discussion and Noriko Fujisawa for secretarial assistance. This study was supported by Grants-in-Aid for Scientific Research from the Ministry of Education, Science, Sports, and Culture of Japan to MO (No. 16390113).

REFERENCES

1. Hozumi N, Tonegawa S. Evidence for somatic rearrangement of immunoglobulin genes coding for variable and constant regions. Proc Natl Acad Sci USA 1976;73:3628–32.
2. Honjo T, Kataoka T. Organization of immunoglobulin heavy chain genes and allelic deletion model. Proc Natl Acad Sci USA 1978;75:2140–4.
3. Seidman JG, Leder P. The arrangement and rearrangement of antibody genes. Nature 1978;276:790–5.
4. Kataoka T, Kawakami T, Takahashi N, Honjo T. Rearrangement of immunoglobulin gamma 1-chain gene and mechanism for heavy-chain class switch. Proc Natl Acad Sci USA 1980;77:919–23.
5. Davis MM, Calame K, Early PW, Livant DL, Joho R, Weissman IL, et al. An immunoglobulin heavy-chain gene is formed by at least two recombinational events. Nature 1980;283:733–9.
6. Allen RC, Armitage RJ, Conley ME, Rosenblatt H, Jenkins NA, Copeland NG, et al. CD40 ligand gene defects responsible for X-linked hyper-IgM syndrome. Science 1993;259:990–3.
7. DiSanto JP, Bonnefoy JY, Gauchat JF, Fischer A, de Saint Basile G. CD40 ligand mutations in x-linked immunodeficiency with hyper-IgM. Nature 1993;361:541–3.
8. Aruffo A, Farrington M, Hollenbaugh D, Li X, Milatovich A, Nonoyama S, et al. The CD40 ligand, gp39, is defective in activated T cells from patients with X-linked hyper-IgM syndrome. Cell 1993;72:291–300.
9. Muramatsu M, Kinoshita K, Fagarasan S, Yamada S, Shinkai Y, Honjo T. Class switch recombination and hypermutation require activation-induced cytidine deaminase (AID), a potential RNA editing enzyme. Cell 2000;102:553–63.
10. Revy P, Muto T, Levy Y, Geissmann F, Plebani A, Sanal O, et al. Activation-induced cytidine deaminase (AID) deficiency causes the autosomal recessive form of the Hyper-IgM syndrome (HIGM2). Cell 2000;102:565–75.
11. Imai K, Catalan N, Plebani A, Marodi L, Sanal O, Kumaki S, et al. Hyper-IgM syndrome type 4 with a B lymphocyte-intrinsic selective deficiency in Ig class-switch recombination. J Clin Invest 2003;112:136–42.
12. Al-Alem U, Li C, Forey N, Relouzat F, Fondanèche MC, Tavtigian SV, et al. Impaired Ig class switch in mice deficient for the X-linked lymphoproliferative disease gene Sap. Blood 2005;106:2069–75.
13. Thompson A, Timmers E, Schuurman RK, Hendriks RW. Immunoglobulin heavy chain germ-line JH-C mu transcription in human precursor B lymphocytes initiates in a unique region upstream of DQ52. Eur J Immunol 1995;25:257–61.
14. Reth MG, Alt FW. Novel immunoglobulin heavy chains are produced from DJH gene segment rearrangements in lymphoid cells. Nature 1984;312:418–23.
15. Alt FW, Rosenberg N, Enea V, Siden E, Baltimore D. Multiple immunoglobulin heavy-chain gene transcripts in Abelson murine leukemia virus-transformed lymphoid cell lines. Mol Cell Biol 1982;2:386–400.
16. Berton MT, Uhr JW, Vitetta ES. Synthesis of germ-line gamma 1 immunoglobulin heavy-chain transcripts in resting B cells: induction by interleukin 4 and inhibition by interferon gamma.Proc Natl Acad Sci USA 1989;86:2829–33.
17. Lutzker S, Rothman P, Pollock R, Coffman R, Alt

FW. Mitogen- and IL-4-regulated expression of germ-line Ig gamma 2b transcripts: evidence for directed heavy chain class switching. Cell 1988;53: 177–84.
18. Stavnezer J, Radcliffe G, Lin YC, Nietupski J, Berggren L, Sitia R, et al. Immunoglobulin heavy-chain switching may be directed by prior induction of transcripts from constant-region genes. Proc Natl Acad Sci USA 1988;85:7704–8.
19. Lebman DA, Nomura DY, Coffman RL, Lee FD. Molecular characterization of germ-line immunoglobulin A transcripts produced during transforming growth factor type beta-induced isotype switching. Proc Natl Acad Sci USA 1990;87:3962–6.
20. Takahashi S, Itoh J, Nose M, Ono M, Yamamoto T, Kyogoku M. Cloning and cDNA sequence analysis of nephritogenic monoclonal antibodies derived from an MRL/lpr lupus mouse. Mol Immunol 1993;30:177–82.
21. Ono M, Yamamoto T, Kyogoku M, Nose M. Sequence analysis of the germ-line VH gene corresponding to a nephritogenic antibody in MRL/lpr lupus mice. Clin Exp Immunol 1995;100:284–90.
22. Ono M, Yamamoto T, Nose M. A simple method based on PCR for detecting the relative mRNA amounts of the four mouse IgG subclasses. J Immunol Methods 1995;184:63–9.
23. Kaartinen M, Makela O. Reading of D genes in variable frames as a source of antibody diversity. Immunol Today 1985;6:324–27.
24. Gu H, Kitamura D, Rajewsky K. B cell development regulated by gene rearrangement: arrest of maturation by membrane-bound D mu protein and selection of DH element reading frames. Cell 1991;65:47–54.
25. Kompfner E, Oliveira P, Montalbano A, Feeney AJ. Unusual germline DSP2 gene accounts for all apparent V-D-D-J rearrangements in newborn, but not adult, MRL mice. J Immunol 2001;167: 6933–8.
26. Feeney AJ. Lack of N regions in fetal and neonatal mouse immunoglobulin V-D-J junctional sequences. J Exp Med 1990;172:1377–90.
27. Macpherson AJ, Gatto D, Sainsbury E, Harriman GR, Hengartner H, Zinkernagel RM. A primitive T cell-independent mechanism of intestinal mucosal IgA responses to commensal bacteria. Science 2000;288:2222–6.
28. Macpherson AJ, Lamarre A, McCoy K, Harriman GR, Odermatt B, Dougan G, et al. IgA production without mu or delta chain expression in developing B cells. Nat Immunol 2001;2:625–31.
29. Fagarasan S, Kinoshita K, Muramatsu M, Ikuta K, Honjo T. In situ class switching and differentiation to IgA-producing cells in the gut lamina propria. Nature 2001;413:639–43.
30. Cazac BB, Roes J. TGF-beta receptor controls B cell responsiveness and induction of IgA in vivo. Immunity 2000;13:443–51.
31. Iwasato T, Arakawa H, Shimizu A, Honjo T, Yamagishi H. Biased distribution of recombination sites within S regions upon immunoglobulin class switch recombination induced by transforming growth factor beta and lipopolysaccharide. J Exp Med 1992;175:1539–46.
32. Park SR, Seo GY, Choi AJ, Stavnezer J, Kim PH. Analysis of transforming growth factor-beta1-induced Ig germ-line gamma2b transcription and its implication for IgA isotype switching. Eur J Immunol 2005;35:946–56.
33. Takahashi S, Nose M, Sasaki J, Yamamoto T, Kyogoku M. IgG3 production in MRL/lpr mice is responsible for development of lupus nephritis. J Immunol 1991;147:515–9.

Biochimica et Biophysica Acta 1778 (2008) 1423–1428

Contents lists available at ScienceDirect

Biochimica et Biophysica Acta

journal homepage: www.elsevier.com/locate/bbamem

Molecular dynamics simulation of structural changes of lipid bilayers induced by shock waves: Effects of incident angles

Kenichiro Koshiyama [a,*], Tetsuya Kodama [b], Takeru Yano [c], Shigeo Fujikawa [d]

[a] Graduate School of Engineering Science, Osaka University, Toyonaka, 560-8531, Japan
[b] Graduate School of Biomedical Engineering, Tohoku University, Sendai, 980-8575, Japan
[c] Graduate School of Engineering, Osaka University, Suita, 565-0871, Japan
[d] Graduate School of Engineering, Hokkaido University, Sapporo, 060-8628, Japan

ARTICLE INFO

Article history:
Received 12 November 2007
Received in revised form 7 March 2008
Accepted 12 March 2008
Available online 20 March 2008

Keywords:
Acoustic wave
Cell membrane permeabilization
Impulse
Shear force
Sonoporation
Ultrasound

ABSTRACT

Unsteady and nonequilibrium molecular dynamics simulations of the response of dipalmitoylphosphatidylcholine (DPPC) bilayers to the shock waves of various incident angles are presented. The action of an incident shock wave is modeled by adding a momentum in an oblique direction to water molecules adjacent to a bilayer. We thereby elucidate the effects of incident shock angles on (i) collapse and rebound of the bilayer, (ii) lateral displacement of headgroups, (iii) tilts of lipid molecules, (iv) water penetration into the hydrophobic region of the bilayer, and (v) momentum transfer across the bilayer. The number of water molecules delivered into the hydrophobic region is found to be insensitive to incident shock angles. The most important structural changes are the lateral displacement of headgroups and tilts of lipid molecules, which are observed only in the half of the bilayer directly exposed to a shock wave for all incident shock angles studied here. As a result, only the normal component of the added oblique momentum is substantially transferred across the bilayer. This also suggests that the irradiation by shock waves may induce a jet-like streaming of the cytoplasm toward the nucleus.

1. Introduction

The cell membrane permeabilization technique utilizing mechanical forces due to high-intensity acoustic waves (shock wave or ultrasound) is a promising method of noninvasive drug and gene delivery into the cytoplasm [1–5]. For the last decade, several authors have addressed the permeabilization mechanisms, in vitro and in vivo, which are fundamental for the complete development of drug and gene delivery methods based on shock waves or ultrasound [6–14]. They have reported that cavitation-induced nonthermal effects (e.g., radiation force, micro-streaming, micro-jets, or shock waves from cavitation bubbles) can induce reversible lesions of cell membranes, and the cell membranes are thereafter permeabilized [6–14].

The above mentioned studies are limited to the macroscopic or cellular level. At the microscopic or molecular level, on the other hand, the mechanisms of the permeabilization induced by shock waves or ultrasound are not well understood. Recently, we conducted molecular dynamics (MD) simulations of the structural changes of phospholipid bilayers of cell membranes induced by the action of shock waves [15]. One of the important findings was that the resulting collapse and rebound of a bilayer are followed by the penetration of water molecules into the hydrophobic region of the bilayer.

In the simulations, the propagation direction of the applied incident shock waves was parallel to the bilayer normal direction. However, bilayers are generally undulating on a length scale well beyond their thickness [16]. That is, the incident shock angles on the membrane surface practically vary with the location on the surface where the shock wave impacts. Furthermore, a numerical analysis in fluid dynamics [17] points out that an oblique impact of a shock wave induces a kind of shear flow around cell membranes and the forces resulting from the flow field are responsible for cell deformation and lysis. The effects of the incident shock angles on the structural changes of a lipid bilayer underlie the permeabilization mechanisms at the molecular level. Therefore, the objective of this study is to analyze the structural changes of a lipid bilayer by using the shock waves of various incident shock angles.

The foundation of all biological membranes is the lipid bilayer structure consisting of two leaflets of phospholipids. Thus, their dynamics (i.e., rearrangement of the phospholipids) is central to understanding the behavior of biological membranes. MD simulations of lipid bilayers have provided accurate models of biological membranes at the nanometer and nanosecond scales [18–21], and the molecular behaviors of lipids, water, and membrane proteins in equilibrium states have been clarified [18,22–25]. Moreover, the studies on the lipid bilayer responses to surface area changes [26], mechanical stresses [27], electric fields [28–30], and shear flows [31–33] are beginning to be conducted.

* Corresponding author. Department of Mechanical Science and Bioengineering, Graduate School of Engineering Science, Osaka University, Toyonaka, 560-8531, Japan. Tel.: +81 6 6850 6173; fax: +81 6 6850 6172.
E-mail address: koshiyama@me.es.osaka-u.ac.jp (K. Koshiyama).

0005-2736/$ – see front matter © 2008 Elsevier B.V. All rights reserved.
doi:10.1016/j.bbamem.2008.03.010

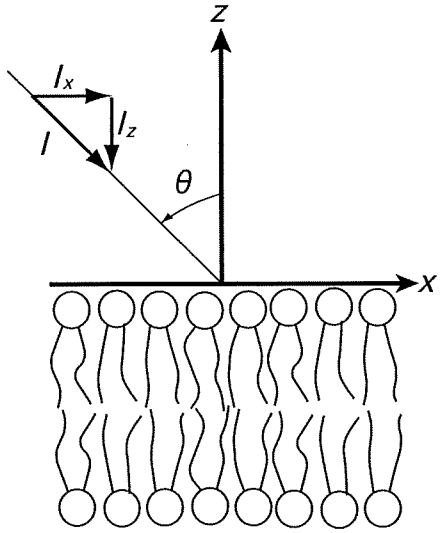

Fig. 1. Schematic diagram of the interaction of a shock wave with a lipid bilayer, where θ is the incident angle between the bilayer normal and the direction of shock wave propagation.

However, these studies involve responses in the steady or almost steady states. We emphasize that a shock wave is a high-pressure wave with a steep wave front that propagates at a supersonic speed, and it passes the cell membrane within a very short time of the order of picoseconds. Therefore, understanding the high-speed phenomenon induced by the interaction of a shock wave with a lipid bilayer should be indispensable. We address the lipid bilayer responses not to steady but unsteady actions induced by shock waves, particularly focusing on the effect of various incident shock angles.

In the previous study [15], we have modeled a shock wave by its impulse and performed unsteady and nonequilibrium MD simulations. Here, we slightly modify the shock wave impulse model to take account of incident shock angles, and the modified model is described in the Methods section. In the Results section, the collapse stage and the rebound stage are defined, and then the lateral displacement of headgroups, tilts of lipid molecules, water penetration into the hydrophobic region of a bilayer, and the momentum transfer across the bilayer are analyzed in detail. We finally summarize the effects of incident shock angles on the structural changes of a bilayer and discuss possible streaming in the cytoplasm induced by shock waves in the Summary and discussion section.

2. Methods

2.1. Lipid bilayer system

In this study, we investigated the effect of the incident angle of a shock wave on a lipid bilayer distributed on a plane surface (see Fig. 1). The lipid bilayer system comprised 128 DPPC molecules fully hydrated by 16455 water molecules. For equilibration, we performed 20-ns simulations with our force fields (see below) in a constant *NPT* ensemble, and we obtained the equilibrated bilayer system of volume $6.56\times6.40\times15.90$ nm^3, where the linear dimension of the simulation box in the z direction normal to the bilayer plane (the xy plane) is 15.90 nm. The detailed simulation procedures for the bilayer equilibration are summarized elsewhere [15,19]. We remark that our system included a large water layer of thickness about 12 nm, whereas the thickness of the bilayer was about 4 nm. This is because this simulation of a shock wave required a large number of water molecules, as explained below.

The force fields for DPPC and water were consistent with those employed in the previous study [15], which includes the refined united atom force field with AMBER99 force field [19] and single point charge (SPC) model [34]. The partial charges of a DPPC molecule were obtained from the study by Chiu et al. [35]. Because we are interested in the dynamical process of a structural change in a bilayer resulting from shock wave irradiation, it may be better to remove the constraints of molecular bond lengths, angles, and dihedrals. Therefore, all bonded interactions in DPPC molecules were calculated in the shock wave simulation. The particle mesh Ewald method [36] was used to treat the long-range electrostatic interactions. Both the real-space Ewald and the van der Waals nonbonded interactions were cut off at 1.0 nm. The AMBER 8 set of programs [37] was used for computations.

2.2. Shock wave impulse simulation

As demonstrated in the previous study [15], we modeled a shock wave by its impulse I defined as the time integral of pressure over the shock-pulse duration [7]. From the definition of the impulse, the shock impulse I can be regarded as an increment in the momentum of water divided by an area A on which the shock pressure is exerted. The momentum increment is numerically implemented by the addition of the average velocity V to the thermal velocity of water molecules in a slab adjacent to a bilayer. V is given by

$$V = \frac{I \times A}{mN_W}, \tag{1}$$

where m is the weight of a water molecule and N_W is the number of water molecules in the water slab.

Because the choice of a water slab is arbitrary, we consider the water slab of $A\times L_z$, where $A=42.2$ nm^2 was the area of the xy plane of the bilayer system and $L_z=4.0$ nm was the thickness of the water slab. We set $I=40$ mPa·s and the number of water molecules in the water slab $N_W=5423$; the applied average velocity V was 10,394 m/s. Note that V corresponds neither to the sound speed in liquid water nor to the propagation speed of the shock wave. It just represents the increase in the momentum of water molecules due to the shock wave.

In the present study, we slightly modified the shock wave model described above to take account of the incident shock angle. More precisely, the shock wave impulse was divided into the normal (in the z direction) and tangential (in the x direction) components to the bilayer plane (see Fig. 1). That is,

$$I_z = I\cos\theta \quad \text{and} \quad I_x = I\sin\theta, \tag{2}$$

where I_z is the normal component; I_x, the tangential component; and θ, the incident shock angle. V was decomposed to the normal component $V_z=V\cos\theta$ and the tangential component $V_x=V\sin\theta$.

For understanding high-speed and unsteady phenomenon induced by a shock wave impulse in MD, position and velocity scaling of molecules should not be implemented. Therefore, we performed constant *NVE* MD simulation without using the temperature and pressure controls and bond constraints from the initial configuration. The constant energy in this MD is the sum of the total energy in the equilibrium state and the kinetic energy increase induced by adding velocity. Periodic boundary conditions were applied in the three directions. The time step used for the integration of equations of motion was 0.2 fs in order to avoid the excess approach of molecules with large velocities. Owing to the periodic boundary conditions, the simulations were terminated at the time when the effect of the shock impulse reached the boundary at the opposite side of the simulation box in the z direction. This is the reason why we prepared a thick water layer. The numerical results shown in the following are the sample averages of 10 production runs for a given θ. From the results of the previous study and preliminary calculations, the system size and the simulation time in the present study were determined in order to focus on the analysis of the essential part of the structural changes in unsteady states.

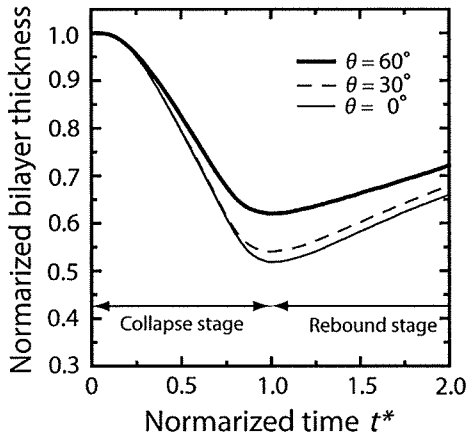

Fig. 2. Temporal changes of the bilayer thickness in the simulations for $\theta=0°$, 30°, and 60°. The bilayer thickness is normalized by that in the initial state (ca. 4.0 nm). Note that in the following figures the normalized time $t^*=1$ corresponds to 530, 590, and 810 fs in real time for $\theta=0°$, 30°, and 60°, respectively.

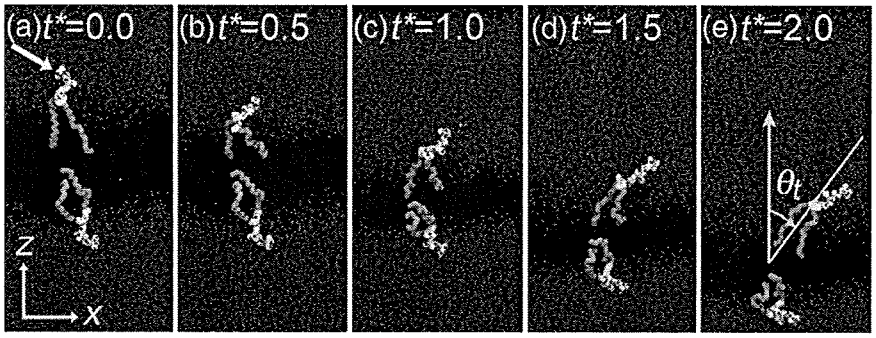

Fig. 3. Snapshots of postural changes of typical lipid molecules in upper and lower layers induced by the shock wave with θ=60°. The yellow bars represent the headgroup of a lipid molecule; the orange bars, the hydrophobic chains; and the red spheres, water molecules. The yellow arrow in the snapshot of t^*=0 denotes the propagation direction of the incident shock wave. The other lipid molecules are eliminated for clarity.

2.3. Analysis

The changes of hydrophobic chains in the unsteady states can be explained in terms of an averaged instantaneous chain order parameter $\hat{S}_{CD}$ [15],

$$\hat{S}_{CD} = -\frac{1}{2}\left(\frac{1}{N_C}\sum_{i=1}^{N_C}\frac{1}{2}(3\cos^2\Theta_i - 1)\right), \quad (3)$$

where Θ_i is the angle between the axis of the ith molecular axis and the bilayer normal (the z axis) and N_C (=28) is the number of carbons in both *sn*-1 and *sn*-2 chains. Θ_i is evaluated from the instantaneous configurations of lipid molecules. Note that Θ_i in the upper layer is calculated with respect to the bilayer director as pointed out in Ref. [31], because the lipid molecules in the upper layer tilt (see the Results section).

The lateral movement of lipid molecules is characterized by the averaged lateral displacement of the mass center positions of the headgroups of lipid molecules $L(t)$ defined by

$$L(t) = \frac{1}{N_L}\sum_{i=1}^{N_L}|x_i(t) - x_i(0)|, \quad (4)$$

where x_i is the x coordinate of the mass center position of the headgroup of the ith molecule, and N_L(=64) is the number of DPPC molecules in the upper or lower layer.

3. Results

3.1. Collapse and rebound of bilayers

The most outstanding change in a bilayer by the action of a shock wave is the change in the bilayer thickness, which is defined as the distance between the phosphorus atoms of lipid molecules in the upper and lower layers [15]. Fig. 2 shows the temporal changes of the bilayer thickness caused by the shock wave impulses of 40 mPa·s for θ=0°, 30°, and 60°. The bilayer thickness became minimum at 530, 590, and 810 fs for θ=0°, 30°, and 60°, respectively. The normalized time t^* in Fig. 2 is defined such that the minimum of bilayer thickness occurs at t^*=1. That is, the bilayer thickness is decreasing during $0<t^*<1$ (i.e., collapse stage); then, the bilayer thickness starts to increase after t^*=1 (i.e., rebound stage) regardless of the incident shock angle conditions. In the following the normalized time t^*=1 corresponds to 530, 590, and 810 fs in real time for θ=0°, 30°, and 60°, respectively.

In each incident angle condition, the duration of the rebound stage ($1<t^*$) is longer than that of the collapse stage ($0<t^*<1$). The rebound stage was not completed within the present simulation because of the periodic boundary conditions (see the Methods section). However, the essential points can be clarified as demonstrated below.

The change in the bilayer thickness is expected to be due to the postural changes of lipid molecules. In Fig. 3, we show a series of snapshots of postural changes of typical lipid molecules in the upper and lower layers induced by the shock wave with θ=60°. By the action of the shock wave, the hydrophobic chains bend (Fig. 3(a)–(c)) and then slightly recover (Fig. 3(d) and (e)). Fig. 4 shows temporal changes of $\hat{S}_{CD}$ for θ=60°, normalized by those in the initial state (ca. −0.16). The order parameters obviously decrease in the collapse stage and gradually recover in the rebound stage. On comparison with the result in Fig. 2, it is confirmed that the decrease in the bilayer thickness was due to this chain disorder. This result is consistent with the previous simulation result [15].

3.2. Lateral movement of lipid molecules

The oblique incidence of a shock wave yields unsteady shear on the bilayer surface. In this simulation, the shear is induced by the tangential momentum change of water molecules adjacent to the bilayer surface (see the Methods section). In Fig. 3, the effect of shear appears as the lateral movement of the lipid molecules in the upper layer. Fig. 5 shows the time evolution of the averaged lateral displacements in the upper and lower layers. As pointed out in the previous study [15], the simple shock wave interaction (θ=0°) enhances the lateral displacement. However, the displacement in the upper layer significantly increases with the incident shock angle from 0° to 60°. In fact, the displacement induced by the shock wave with θ=60° becomes 1.5 nm at t^*=2, which is ten times larger than that with θ=0°. Here, we remark that the lateral displacements of lipid molecules for θ=30° and 60° continue to increase even in the rebound stage. On the other hand, the lateral displacement in the lower layer is one order of magnitude smaller than that in the upper layer (Fig. 5 inset).

3.3. Tilt of lipid molecules

From the snapshots in Fig. 3, it is clear that the lipid molecule in the upper layer tilts by the action of incident shock wave. Here, we define the tilt angle as follows: (i) atom positions of a lipid molecule are projected onto the xz plane; (ii) a straight line is fitted to these projected

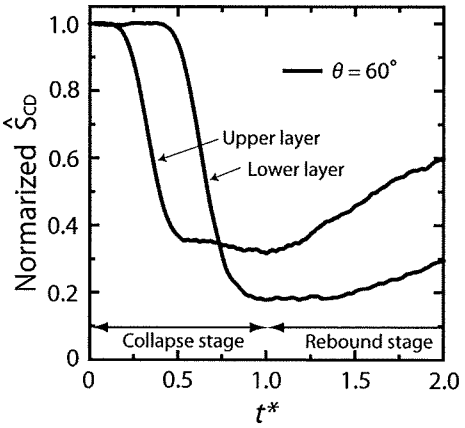

Fig. 4. Temporal changes of averaged instantaneous order parameter for θ=60°. The order parameters are normalized by those in the initial state.

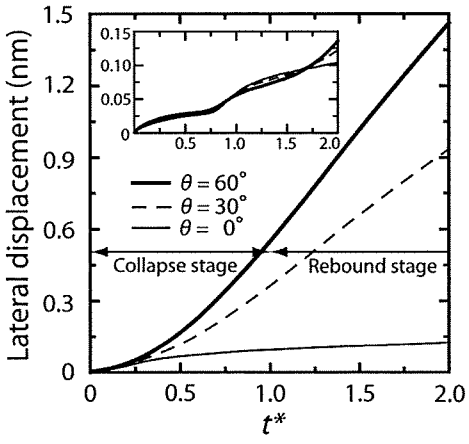

Fig. 5. Lateral displacement of the mass center of lipid headgroups for θ=0°, 30°, and 60° in the upper layer and that in the lower layer (inset).

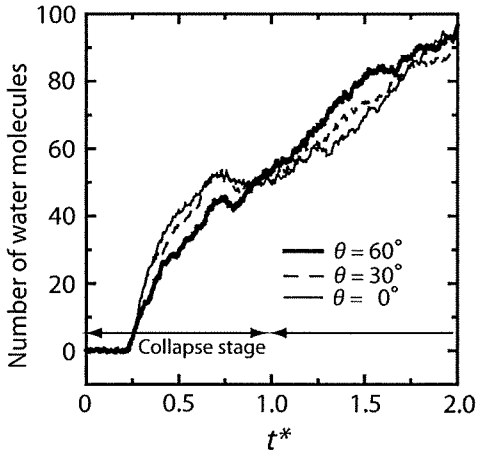

Fig. 7. Number of the water molecules delivered into the hydrophobic region of a bilayer induced by shock wave with θ=0°, 30°, and 60°.

positions; (iii) the tilt angle θ_t is obtained from the angle formed between this straight line and the z axis (see Fig. 3(e)). The tilt angle in the initial state (t^*=0) calculated here has a wide distribution centered around zero degree, which would be tantamount to that in the equilibrium state of another study [24] although they used a different force field and their tilt angle is defined as that between a vector formed by alternating carbon units along the lipid tails and the bilayer normal axis.

Fig. 6(a) shows the tilt angle distributions of the lipid molecules in the upper layer at t^*=2. In the case of θ=0°, the distribution of tilt angles is hardly changed from that in the initial state. On the contrary, the distributions for θ=30° and 60° shift to the positive side. In Fig. 6 (b), we show the temporal changes of the tilt angles averaged for all lipid molecules in the upper layer. Obviously, the averaged tilt angles for θ=30° and 60° increase with time and reach maximum values at around t^*=2 (21°, and 32°, respectively). The maximum values are in agreement with those in Ref. [31] on the interaction of steady shear flows with lipid bilayers. In the present unsteady simulation, the lipid alignment is completed within t^*=2. Thus, the simulation limited to $0<t^*<2.0$ is adequate to analyze the essential part of the structural changes in unsteady states. Interestingly, whereas the lateral movement of lipid molecules persists as shown in Fig. 5, their tilts are saturated (Fig. 6(b)). However, this will not be discussed in this paper.

The tilt angles averaged in the lower layer did not change (data not shown). We emphasize that this is not due to the restriction of simulation time because the steady simulation of shear flow also obtained the same result [31].

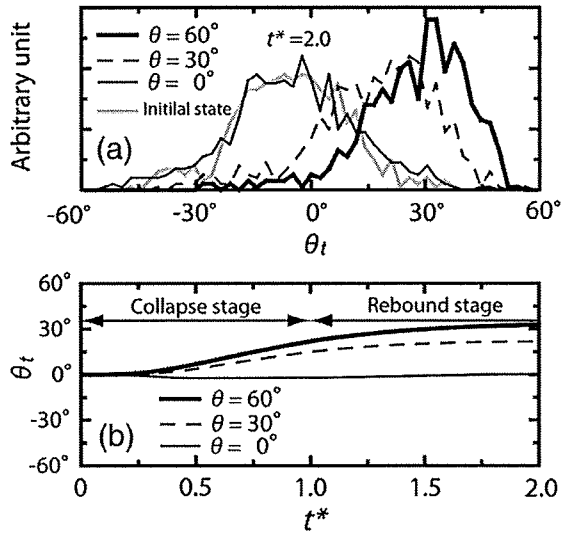

Fig. 6. (a) Tilt angle distributions of the lipid molecules in the upper layer for θ=0°, 30°, and 60° at t^*=2.0 (b) Temporal changes of the averaged tilt angle of lipid molecules in the upper layer. Note that the average equilibrium angle in the initial state is taken as 0° in (b).

3.4. Water penetration into the hydrophobic region

In the equilibrium state water molecules hardly exist in the hydrophobic region [18] and the event of water penetration into the hydrophobic region rarely occurs in the time scale of MD simulations [38,39]. On the other hand, under the action of shock waves the water penetration into the hydrophobic region was observed in the time scale of picoseconds (see Fig. 3), which is important for subsequent water pore formation in a bilayer [40] and cell membrane permeabilization [4,6,9,15]. Fig. 7 shows the temporal changes of the number of water molecules delivered into the hydrophobic region for θ=0°, 30°, and 60°. Here, the hydrophobic region is defined as the region between the carbonyl groups in *sn*-1 chains in the upper and lower layers [15]. Most of the water molecules penetrated are from the upper water layer. The water penetration in the intermediate stage of

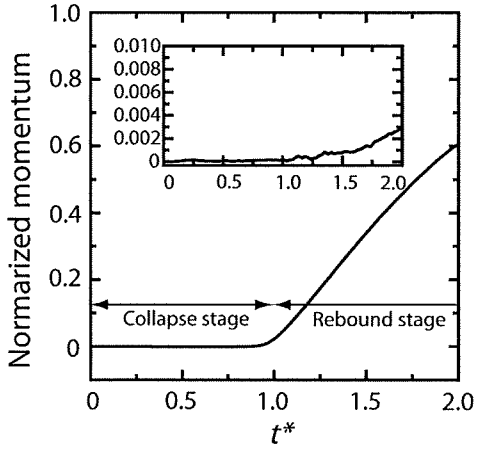

Fig. 8. Temporal changes of the momentum of the lower water layer in the z direction (normal component) and that in the x direction (tangential component, inset) for θ=60°.

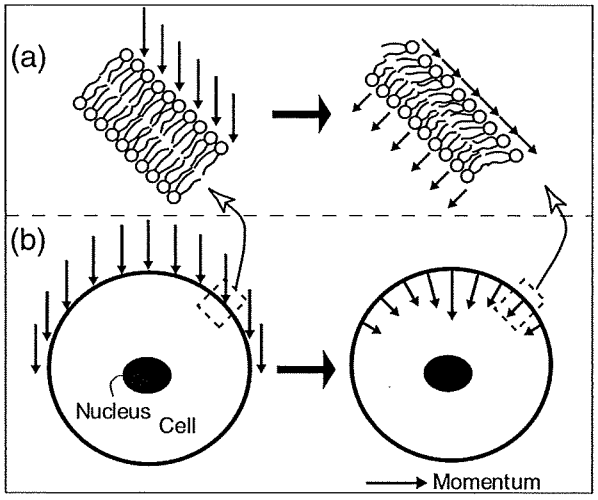

Fig. 9. Schematic diagram of (a) structural changes of cell membranes and (b) expected momentum transfer across the membrane in a cell by shock waves.

the collapse stage ($0.25<t^*<0.75$) is smaller in the larger incident angle condition. By contrast, in the intermediate stage of the rebound stage ($1.25<t^*<1.75$), the water penetration is larger in the larger incident angle condition. As a result, the total number of delivered water molecules amounts to almost 100 for all cases of $\theta=0°$, 30°, and 60°, indicating the fact that the water penetration in $0<t^*<2.0$ is insensitive to the incident angles, at least for the case of $I=40$ mPa·s.

The trend in the collapse stage is clearly a direct consequence of the difference in the impulse intensity in the normal direction. In the rebound stage, on the other hand, a large amount of the normal component of the momentum has been transferred through the upper layer, as shown in the next subsection; instead, the lateral displacements and tilts of lipid molecules in the upper layer are prominent as demonstrated in Figs. 5, and 6. Therefore, the penetration of water molecules near the upper layer in the rebound stage may be governed by these lipid structural changes [23,25,41].

3.5. Momentum transfer across bilayers

It is interesting to assess the amount of momentum transferred across the bilayer by the shock wave because the momentum transfer is related to the transfer characteristics of the bilayer or a subsequent flow induction. The momentum transfer can be estimated from the changes of momentum in the lower water layer. In Fig. 8, we show temporal changes of the normal and tangential components of momentum for $\theta=60°$ normalized by the corresponding values initially added to the water slab. Both the components begin to increase at around $t^*=1.0$, and in particular, the normal component attains 60% of its initial value at $t^*=2.0$, while the increase in the tangential component remains very small. That is, only the normal component of the added oblique momentum is substantially transferred across the bilayer within the time scale of the order of picoseconds. This certainly affects the flow induction in the cytoplasm and this will be discussed in detail in the final section. Note that the rest of the normal component, 40% of its initial value, still stays inside the bilayer at $t^*=2.0$ as can be seen from Fig. 3(e), where the downward movement of lipid molecules persists.

The ratio between the sliding force per unit of bilayer area and the velocity difference between the two leaflets of a bilayer is called the intermonolayer friction coefficient b, which is one of the measures of the intermonolayer flow behavior [32,33,42]. b is given by $b=F/A\Delta V$, where F is the sliding force, A is the bilayer area, and ΔV is the velocity difference. Usually, b is evaluated in lengthy steady simulations, however, it can be obtained in an unsteady simulation as follows: F for $\theta=60°$ was roughly calculated from the momentum change of the lower layer (17753.06 N·s/mol) divided by the time interval $0<t^*<2.0$ (1.56 ps); the sliding force between the lower monolayer and lower water layer was assumed to be zero because of the very small amount of momentum transferred to the lower water layer (Fig. 8 inset); the slip velocity was the instantaneous velocity difference of the mass centers of the upper and lower layers at $t^*=2.0$ (571.74 m/s). As a result, we obtained $b=8\times10^5$ Pa m^{-1}s at $t^*=2.0$ in the unsteady state using the present simulation results. Surprisingly, the intermonolayer friction coefficient in the present study is almost the same as that obtained in the coarse-grained MD simulations in Refs. [32,33] (typically 1×10^6 Pa m^{-1}s) by applying Lees–Edwards boundary conditions, although the normal component of momentum was not considered in these simulations.

4. Summary and discussion

This study aimed at investigating the effect of incident shock angles on the structural changes of a lipid bilayer by using unsteady nonequilibrium MD simulations. The simulation results revealed that the half of the bilayer directly exposed to shock waves is sensitive to an incident shock wave; therefore, the lateral displacement and the tilts of lipid molecules are enhanced with an increase in the incident shock angle from 0° to 60° within the time scale of the order of picoseconds (Fig. 9(a)). On the other hand, the other half of the bilayer is found to be insensitive to the change of the incident shock angle. This difference in sensitivity to the incident shock wave results in the fact that only the normal component of the applied oblique impulse is transferred across the bilayer.

Finally, we discuss the possible streaming of the cytoplasm induced by shock waves. As shown in Fig. 8, the normal component of the applied momentum promptly transfers across the bilayer, whereas the tangential component hardly transfers. Here, let us assume a cell to be a sphere and a shock wave impulse is applied downward on the surface of the sphere (Fig. 9(b) left). The intensity of the applied momentum along membrane normal is largest on the top of the sphere, and it is reduced to zero along the meridian of the sphere. Accordingly, the momentum distribution has a maximum (Fig. 9(b) right), which will result in the formation of a jet-like streaming in the cytoplasm. In reality, the cell membrane is usually undulating; hence, several momentum maxima with different directions may be produced beneath the membrane. Therefore, the streaming in the cytoplasm caused by the shock wave will be comprised of several jet-like flows emerged from several momentum maxima, and the entire flow pattern in the cytoplasm will become complex. The mixing or homogenization of plasmid [10] and fluorescein [7] throughout the cell cytoplasm appears to be enhanced by jet-like flows.

Acknowledgements

TK acknowledges (i) the Encouraging Development of Strategic Research Center, Special Coordination Funds for Promoting Science and Technology, MEXT, Japan, (ii) Grant-in-Aid for Scientific Research (B) (17300168), (iii) Grant-in-Aid for Exploratory Research (18650140), and (iv) Research on Advanced Medical Technology, The Ministry of Health Labor and Welfare (H19-nano-010).

References

[1] S. Gambihler, M. Delius, Transient increase in membrane permeability of L1210 cells upon exposure to lithotripter shock waves in vitro, Naturwissenschaften 79 (1992) 328–329.
[2] S. Gambihler, M. Delius, J.W. Ellwart, Permeabilization of the plasma membrane of L1210 mouse leukemia cells using lithotripter shock waves, J. Membr. Biol. 141 (1994) 267–275.
[3] U. Lauer, E. Burgelt, Z. Squire, K. Messmer, P.H. Hofschneider, M. Gregor, M. Delius, Shock wave permeabilization as a new gene transfer method, Gene Ther. 4 (1997) 710–715.

[4] L.B. Feril, T. Kondo, S. Umemura, K. Tachibana, H.A. Manalo, P. Riesz, Sound wave and antineoplastic drugs: the possibility of an enhanced combined anticancer therapy, J. Med. Ultrasonics 29 (2002) 173–187.
[5] S. Mehier-Humbert, R.H. Guy, Physical methods for gene transfer: improving the kinetics of gene delivery into cells, Adv. Drug Delivery Rev. 57 (2005) 733–753.
[6] M. Kambe, N. Ioritani, R. Kanamaru, Enhancement of chemotherapeutic effects with focused shock waves: extracorporeal shock wave chemotherapy (ESWC), Hum. Cell 10 (1997) 87–94.
[7] T. Kodama, M.R. Hamblin, A.G. Doukas, Cytoplasmic molecular delivery with shock waves: importance of impulse, Biophys. J. 79 (2000) 1821–1832.
[8] J. Sundaram, B.R. Mellein, S. Mitragotri, An experimental and theoretical analysis of ultrasound-induced permeabilization of cell membranes, Biophys. J. 84 (2003) 3087–3101.
[9] S. Mehier-Humbert, T. Bettinger, F. Yan, R.H. Guy, Plasma membrane poration induced by ultrasound exposure: implication for drug delivery, J. Contr. Rel. 104 (2005) 213–222.
[10] S. Mehier-Humbert, T. Bettinger, F. Yan, R.H. Guy, Ultrasound-mediated gene delivery: kinetics of plasmid internalization and gene expression, J. Contr. Rel. 104 (2005) 203–211.
[11] T. Kodama, Y. Tomita, K.I. Koshiyama, M.J.K. Blomley, Transfection effect of microbubbles on cells in superposed ultrasound waves and behavior of cavitation bubble, Ultrasound in Med. Biol. 32 (2006) 905–914.
[12] W.D. O'Brien Jr., Ultrasound-biophysics mechanisms, Prog. Biophys. Mol. Biol. 93 (2007) 212–255.
[13] D.L. Miller, Overview of experimental studies of biological effects of medical ultrasound caused by gas body activation and inertial cavitation, Prog. Biophys. Mol. Biol. 93 (2007) 314–330.
[14] E. VanBavel, Effects of shear stress on endothelial cells: possible relevance for ultrasound applications, Prog. Biophys. Mol. Biol. 93 (2007) 374–383.
[15] K. Koshiyama, T. Kodama, T. Yano, S. Fujikawa, Structural change in lipid bilayer and water penetration induced by shock wave: molecular dynamics simulations, Biophys. J. 91 (2006) 2198–2205.
[16] U. Seifert, Configurations of fluid membranes and vesicles, Adv. Phys. 46 (1997) 13–137.
[17] M. Lokhandwalla, B. Sturtevant, Mechanical haemolysis in shock wave lithotripsy (SWL): I. Analysis of cell deformation due to SWL flow-fields, Phys. Med. Biol. 46 (2001) 413–437.
[18] D.P. Tieleman, S.J. Marrink, H.J.C. Berendsen, A computer perspective of membranes: molecular dynamics studies of lipid bilayer systems, Biochim. Biophys. Acta-Rev. Biomemb. 1331 (1997) 235–270.
[19] A.M. Smondyrev, M.L. Berkowitz, United atom force field for phospholipid membranes: constant pressure molecular dynamics simulation of dipalmitoylphosphatidicholine/water system, J. Comp. Chem. 20 (1999) 531–545.
[20] C. Anezo, A.H. de Vries, H.D. Holtje, D.P. Tieleman, S.J. Marrink, Methodological issues in lipid bilayer simulations, J. Phys. Chem., B 107 (2003) 9424–9433.
[21] M. Patra, M. Karttunen, M.T. Hyvonen, E. Falck, P. Lindqvist, I. Vattulainen, Molecular dynamics simulations of lipid bilayers: major artifacts due to truncating electrostatic interactions, Biophys. J. 84 (2003) 3636–3645.
[22] W.L. Ash, M.R. Zlomislic, E.O. Oloo, D.P. Tieleman, Computer simulations of membrane proteins, Biochim. Biophys. Acta-Rev. Biomemb. 1666 (2004) 158–189.
[23] M. Kupiainen, E. Falck, S. Ollila, P. Niemela, A.A. Gurtovenko, M.T. Hyvonen, M. Patra, M. Karttunen, I. Vattulainen, Free volume properties of sphingomyelin, DMPC, DPPC, and PLPC bilayers, J.Comp. Theor. Nanosci. 2 (2005) 401–413.
[24] S. Leekumjorn, A.K. Sum, Molecular studies of the gel to liquid–crystalline phase transition for fully hydrated DPPC and DPPE bilayers, Biochim. Biophys. Acta-Biomemb. 1768 (2007) 354–365.
[25] K. Murzyn, W. Zhao, M. Karttunen, M. Kurdziel, T. Rog, Dynamics of water at membrane surfaces: effect of headgroup structure, Biointerphases 1 (2006) 98–105.
[26] J.G. Jeon, G.A. Voth, The dynamic stress responses to area change in planar lipid bilayer membranes, Biophys. J. 88 (2005) 1104–1119.
[27] H. Leontiadou, A.E. Mark, S.J. Marrink, Molecular dynamics simulations of hydrophilic pores in lipid bilayers, Biophys. J. 86 (2004) 2156–2164.
[28] D.P. Tieleman, The molecular basis of electroporation, BMC Biochem. 5 (2004) 1–10.
[29] Q. Hu, S. Viswanadham, R.P. Joshi, K.H. Schoenbach, S.J. Beebe, P.F. Blackmore, Simulations of transient membrane behavior in cells subjected to a high-intensity ultrashort electric pulse, Phys. Rev., E 71 (2005) 0319141–0319149.
[30] M. Tarek, Membrane electroporation: a molecular dynamics simulation, Biophys. J. 88 (2005) 4045–4053.
[31] P.D. Blood, G.S. Ayton, G.A. Voth, Probing the molecular-scale lipid bilayer response to shear flow using nonequilibrium molecular dynamics, J. Phys. Chem., B 109 (2005) 18673–18679.
[32] S.A. Shkulipa, W.K. den Otter, W.J. Briels, Surface viscosity, diffusion, and intermonolayer friction: simulating sheared amphiphilic bilayers, Biophys. J. 89 (2005) 823–829.
[33] W.K. den Otter, S.A. Shkulipa, Intermonolayer friction and surface shear viscosity of lipid bilayer membranes, Biophys. J. 93 (2007) 423–433.
[34] H.J.C. Berendsen, J.P.M. Postma, W.F. Gunsteren, J. Hermans, Interaction models for water in relation to protein hydration, in: B. Pullman (Ed.), Intermolecular Forces, D. Reidel Publishing Company, 1981, pp. 331–342.
[35] S.W. Chiu, M. Clark, V. Balaji, S. Subramaniam, H.L. Scott, E. Jakobsson, Incorporation of surface-tension into molecular-dynamics simulation of an interface — a fluid-phase lipid bilayer-membrane, Biophys. J. 69 (1995) 1230–1245.
[36] U. Essmann, L. Perera, M.L. Berkowitz, T. Darden, H. Lee, L.G. Pedersen, A smooth particle mesh Ewald method, J. Chem. Phys. 103 (1995) 8577–8593.
[37] D.A. Pearlman, D.A. Case, J.W. Caldwell, W.S. Ross, T.E. Cheatham, S. Debolt, D. Ferguson, G. Seibel, P. Kollman, Amber, a package of computer-programs for applying molecular mechanics, normal-mode analysis, molecular-dynamics and free-energy calculations to simulate the structural and energetic properties of molecules, Comp. Phys. Comm. 91 (1995) 1–41.
[38] S.J. Marrink, H.J.C. Berendsen, Simulation of water transport through a lipid-membrane, J. Phys. Chem. 98 (1994) 4155–4168.
[39] T.X. Xiang, Translational diffusion in lipid bilayers: dynamic free-volume theory and molecular dynamics simulation, J. Phys. Chem., B 103 (1999) 385–394.
[40] K. Koshiyama, T. Kodama, T. Yano, S. Fujikawa, Molecular dynamics simulation of water pore formation in lipid bilayer induced by shock waves, AIP Conf. Proc. 829 (2006) 583–587.
[41] J. Repakova, P. Capkova, J.M. Holopainen, I. Vattulainen, Distribution, orientation, and dynamics of DPH probes in DPPC bilayer, J. Phys. Chem., B 108 (2004) 13438–13448.
[42] E. Evans, A. Yeung, Hidden dynamics in rapid changes of bilayer shape, Chem. Phys. Lipids 73 (1994) 39–56.

British Journal of Cancer (2007) 97, 170–176

www.bjcancer.com

Clinical Studies

A phase I and pharmacokinetic study of NK105, a paclitaxel-incorporating micellar nanoparticle formulation

T Hamaguchi*[,1], K Kato[1], H Yasui[1], C Morizane[1], M Ikeda[1], H Ueno[1], K Muro[1], Y Yamada[1], T Okusaka[1], K Shirao[1], Y Shimada[1], H Nakahama[2] and Y Matsumura[3]

[1]Department of Medicine National Cancer Center Hospital, 5-1-1 Tsukiji, Chuo-ku, Tokyo 104-0045, Japan; [2]Clinical Trial Coordinating Division, National Cancer Center Hospital, 5-1-1 Tsukiji, Chuo-ku, Tokyo 104-0045, Japan; [3]Investigative Treatment Division, Research Center for Innovative Oncology, National Cancer Center Hospital East, 6-5-1 Kashiwanoha, Kashiwa, 277-8577, Japan

This phase I study was designed to examine the maximum tolerated dose (MTD), the dose-limiting toxicities (DLTs), the recommended dose (RD) for phase II, and the pharmacokinetics of NK105, a new polymeric micelle carrier system for paclitaxel (PTX). NK105 was administered as a 1-h intravenous infusion every 3 weeks, without antiallergic premedication. The starting dose was 10 mg m^{-2}, and the dose was escalated according to the accelerated titration method. Nineteen patients were recruited. The tumour types treated included pancreatic ($n = 11$), bile duct ($n = 5$), gastric ($n = 2$), and colonic ($n = 1$) cancers. Neutropenia was the most common haematological toxicity. A grade 3 fever developed in one patient given 180 mg m^{-2}. No other grades 3 or 4 nonhaematological toxicities, including neuropathy, was observed during the entire study period. DLTs occurred in two patients given 180 mg m^{-2} (grade 4 neutropenia lasting for more than 5 days). Thus, this dose was designated as the MTD. Grade 2 hypersensitivity reactions developed in only one patient given 180 mg m^{-2}. A partial response was observed in one patient with pancreatic cancer. The maximum concentration (C_{max}) and area under the concentration (AUC) of NK105 were dose dependent. The plasma AUC of NK105 at 150 mg m^{-2} was approximately 15-fold higher than that of the conventional PTX formulation. NK105 was well tolerated, and the RD for the phase II study was determined to be 150 mg m^{-2} every 3 weeks. The results of this phase I study warrant further clinical evaluation.

British Journal of Cancer (2007) **97,** 170–176. doi:10.1038/sj.bjc.6603855 www.bjcancer.com
Published online 26 June 2007

Keywords: NK105; paclitaxel; polymer micelles; phase I study; DDS

Paclitaxel (PTX), an antimicrotubule agent, has a wide spectrum of antitumour activity including ovarian, breast, stomach, lung, and head and neck cancers (Rowinsky *et al*, 1990; Carney, 1996; Crown and O'Leary, 2000). The clinically used PTX preparation is a mixture of Cremophor EL and ethanol because of PTX's poor water solubility. However, the use of Cremophor EL is known to be associated with acute hypersensitivity reactions (Weiss *et al*, 1990; Rowinsky and Donehower, 1995; Kloover *et al*, 2004). Other PTX preparations that have been categorised as drug delivery systems (DDS) have also been developed. These preparations include Xyotax (polyglutamate-conjugated PTX; Singer *et al*, 2003; Boddy *et al*, 2005), Abraxane (PTX coated with albumin; Ibrahim *et al*, 2002; Deisai *et al*, 2003; Nyman *et al*, 2005), and Genexol-PM (a PTX micelle in which PTX has been simply solubilised; Kim *et al*, 2004). The common advantage shared by these formulations is that they are injectable intravenously without the mixture of Cremophor EL and ethanol. Among them, Abraxane has been approved for metastatic breast cancer by the Food and Drug Administration in the USA based on the results of a randomised phase 3 trial. In this trial, Abraxane demonstrated significantly higher response rates, compared with standard PTX, and a significantly longer time to progression (Gradishar *et al*, 2005). In addition, the incidence of grade 4 neutropenia was significantly lower for Abraxane than for PTX. However, peripheral sensory neuropathy was more common in the arm (Gradishar *et al*, 2005).

NK105 is a PTX-incorporating 'core-shell-type' polymeric micellar nanoparticle formulation (Hamaguchi *et al*, 2005). This particle can be injected intravenously without the use of Cremophor EL or ethanol as a vehicle. Therefore, NK105 is expected to possess a clinical advantage similar to that of the above-mentioned PTX formulations. The difference between NK105 and the other PTX dosage forms is that NK105 is expected to yield a markedly higher plasma and tumour area under the concentration (AUC), compared with those for the other PTX formulations. Moreover, regarding the toxic profiles, the repeated administration of NK105 to rats at 7-day intervals produced significantly fewer toxic effects on peripheral nerves than free PTX. Macromolecular drugs, including NK105, have been developed based on the characteristic macroscopic features of solid tumours, such as hypervasculature, the presence of vascular permeability factors stimulating extravasation within cancer, and the suppressed lymphatic clearance of macromolecules. These characteristics, which are unique to solid tumours, constitute the basis of the enhanced permeability and retention (EPR) effect (Matsumura and Maeda, 1986; Maeda *et al*, 2000; Duncan, 2003). The *in vivo*

*Correspondence: Dr T Hamaguchi; E-mail: thamaguc@ncc.go.jp
Received 13 March 2007; revised 23 May 2007; accepted 23 May 2007; published online 26 June 2007

antitumour activity of NK105 was significantly more potent than that of free PTX, probably because of enhanced tumour exposure through the EPR effect (Hamaguchi *et al*, 2005).

We conducted a phase I clinical trial using NK105 in patients with advanced solid tumours. The objectives of this trial were to determine the maximum tolerated dose (MTD), the phase II recommended dose (RD), and the pharmacokinetics of NK105.

PATIENTS AND METHODS

The protocol and all materials were approved by the Institutional Review Board of the National Cancer Center, Tokyo. This study was conducted in compliance with the Good Clinical Practice Guidelines of the International Conference on Harmonization and the Declaration of Helsinki Principles. Written informed consent was obtained from all the patients.

Therapeutic agent

NK105 was supplied by Nippon Kayaku Co. Ltd. (Tokyo, Japan) in 20-ml glass vials containing a dose equivalent to 30 mg of PTX. When reconstituted in 10 ml of 5% glucose solution and diluted with a total volume of 250 ml of 5% glucose, the reconstituted solution was stable for 24 h at room temperature. In our preclinical study, DLS and HPLC analysis showed that less than 2% of PTX incorporated in the micelles was released for 24 h at room temperature (data not shown).

Figure 1 shows the schematic structure of NK105, a PTX-entrapped polymeric micelle formulation. The NK105 polymers were constructed using polyethylene glycol (PEG) as the hydrophilic component and modified polyaspartate as the hydrophobic component. PEG is believed to form the outer shell of the micelle, producing a 'stealth' effect that enables NK105 to avoid being captured by the reticuloendothelial system.

The modified polyaspartate chain is hydrophobic and is believed to form the hydrophobic inner core of the micelles in aqueous media. The hydrophobic inner core enables NK105 to entrap a sufficient amount of PTX. NK105 has a diameter of about 90 nm (Hamaguchi *et al*, 2005).

Patients

Patients with solid tumours refractory to conventional chemotherapy and for whom no effective therapy was available were eligible for enrolment in this study, provided that the following criteria were met: a histologically confirmed malignant tumour; a performance status of $\leqslant 2$; an age of $\geqslant 20$ and <75 years; a normal haematological profile (neutrophil count $\geqslant 2000\,mm^{-3}$, platelet count $\geqslant 100\,000\,mm^{-3}$, hemoglobin $\geqslant 9\,g\,dl^{-1}$); normal hepatic function (total bilirubin level $\leqslant 1.5\,mg\,dl^{-1}$, AST and ALT $\leqslant 2.5$ times the upper normal limit); normal renal function (serum creatinine $\leqslant 1.5\,mg\,dl^{-1}$); normal cardiac function (New York Heart Association (NYHA) classification of $\leqslant 1$); normal pulmonary function ($PaO_2 \geqslant 60$ mm Hg); no chemotherapy within 4 weeks (6 weeks for nitrosourea or mitomycin C) of the administration of NK105; and a life expectancy of more than 2 months. Patients with serious infections (including hepatitis B, hepatitis C, or HIV) were ineligible for enrolment in the study. Patients who had been previously treated with a taxane were excluded because of assessing neuropathy. Patients were also excluded if they were pregnant or lactating. Additionally, any patient whom the investigators considered ineligible was excluded.

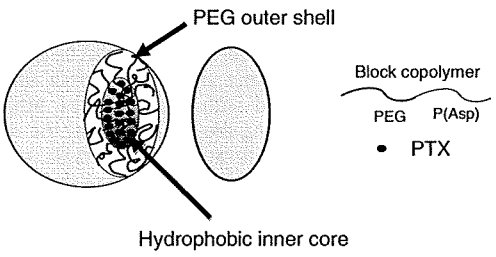

Figure 1 Schematic structure of NK105. A polymeric micelle carrier of NK105 consists of a block copolymer of PEG (molecular weight of about 12 000) and modified polyaspartate. PEG is believed to be the outer shell of the micelle. PEG is believed to form the outer shell of the micelle. NK105 has a highly hydrophobic inner core, and therefore can entrap a sufficient amount of PTX.

Drug administration

NK105 was dissolved in 5% glucose solution for injection at room temperature. NK105 was administered intravenously without in-line filtration and without premedication. NK105 solution was infused using an electric pump at a speed of $250\,ml\,h^{-1}$.

Dosage and dose escalation

The starting dosage of NK105 was $10\,mg\,m^{-2}$, which is one-third of the toxic dose low in dogs. NK105 was administered once every 3 weeks, and the treatment was continued unless a severe adverse event or disease progression was observed. Dose escalation was performed according to the previously described accelerated titration method (Simon *et al*, 1997; Matsumura *et al*, 2004).

Toxicity was graded from 1 to 4 using the National Cancer Institute Common Toxicity Criteria (version 2.0). Intrapatient dose escalation was not permitted. The MTD was defined as the level at which two out of six patients experienced dose-limiting toxicities (DLTs). The recommended dosage for a phase II trial was defined by the Efficacy and Safety Assessment Committee based on the safety, pharmacokinetics, and efficacy results of this trial. DLT was defined as grade 4 neutropenia lasting more than 5 days, a platelet count of less than $25\,000\,\mu l^{-1}$, or grade 3 or higher non-haematological toxicity, with the exception of nausea, vomiting, appetite loss, and hypersensitivity.

Pretreatment assessment and follow-up care

A complete medical history and physical examination, performance status evaluation, complete blood cell count (CBC), blood chemistry, urinalysis, electrocardiogram (ECG), and a computed tomography (CT) examination were performed in each patient. Other examinations were performed only in the presence of a specific clinical indication. Patients were physically examined every day until the second administration of NK105; CBC and blood chemistry tests were performed on day 3 and weekly thereafter. An ECG examination was repeated before each administration of NK105. Tumour marker levels were also measured before every administration. Tumour response was evaluated according to the Response Evaluation Criteria in Solid Tumors criteria (Therasse *et al*, 2000).

Liquid chromatography/tandem mass spectrometry determination of PTX concentrations

The PTX concentrations determined in the present phase I study represented the total drug concentrations (both micelle-entrapped and released). It was difficult to measure released PTX and micelle-entrapped PTX separately, because the equilibrium between both forms could not keep constant during the separating procedure. PTX was extracted from human plasma (0.2 ml) or urine (0.5 ml) by deproteinisation with acetonitrile. The quantifications of PTX in plasma and urine were performed using liquid chromatography/tandem mass spectrometry. Reversed-phase column-switching

chromatography was conducted using an ODS column and detection was enabled by electrospray ionisation of positive mode.

Pharmacokinetic analysis

The following pharmacokinetic parameters were calculated for each patient using a non-compartmental model using the WinNonlin Professional version 4.1 program (Pharsight Corporation, Mountain View, CA, USA). The maximum concentration (C_{max}) was the maximum observed plasma concentration of PTX, and the time-to-the-maximum concentration (T_{max}) was the time corresponding to C_{max}. The area under the concentration (AUC)–time curve from time zero up to the last quantifiable time point (AUC_{0-t}) was calculated using the linear trapezoidal rule, and the area under the concentration–time curve from zero until infinity ($AUC_{0-inf.}$) was calculated as the sum of AUC_{0-t} and the extrapolated area under the zero moment curve from the last quantifiable time point to infinity calculated by dividing the plasma concentration of the last quantifiable time point (observed value) by the elimination rate constant. The half-life of the terminal phase ($t_{1/2Z}$) was calculated as $\log_e 2/\lambda z$, where λz is the elimination rate constant calculated from the terminal linear portion of the log of the concentration in plasma. Total clearance (CL_{tot}), the volume of distribution at steady state (V_{ss}), and renal clearance (CL_r) were calculated using the following equations, where D is the dose and $AUMC_{inf.}$ the area under the first moment curve from time zero until infinity:

$$CL_{tot} = D/AUC_{inf.}$$

$$V_{ss} = AUMC_{inf.}/AUC_{inf.} \times CL_{tot}$$

$$CL_r = \text{cumulative urinary excretion}/AUC_{inf.} / \text{body surface area}$$

RESULTS

Patient characteristics

Nineteen eligible patients were recruited for the study (Table 1). All the patients had received chemotherapy before enrolment. Prior therapies ranged from 1 to 3 regimens of chemotherapy. None of the patients had received taxane chemotherapy. All the patients were included in the safety and response analyses.

Dosing

Dosage escalation started at 10 mg m^{-2} and was increased up to 180 mg m^{-2}. In total, 73 administrations were performed in 19 patients. Eighteen patients received more than two administrations. The maximum number of treatments was 14 courses at 150 mg m^{-2}; the average number of administrations at all levels was 3.8 courses. Up until 80 mg m^{-2}, grade 2 toxicity was not observed during the first course.

According to the original protocol, the dosage of NK105 should have been doubled for each escalation until grade 2 toxicity. However, the safety committee recommended that the dosage should be raised by 40% instead of 100% at 110 mg m^{-2} and that a modified Fibonacci escalation method should be implemented. Therefore, we recruited three patients at dosage level 5 (110 mg m^{-2}) and re-started the dose identification study using a modified Fibonacci method.

Table 1 Patient characteristics

Number of patients	19
Male/female	13/6
Age (years)	
Median	57
Range	43–72
ECOG PS	
Median	0
0	10
1	9
Prior treatment	
Chemotherapy regimens	
Median	1
Range	1–3

Haematological toxicity

Significant myelosuppression was not observed up to level 4 (80 mg m^{-2}). At level 7 (180 mg m^{-2}), two out of five patients appeared to have acquired DLTs, namely grade 4 neutropenia lasting for more than 5 days. On the basis of these results, 180 mg m^{-2} was considered to be the MTD, with neutropenia as the DLT. Since a dosage of 150 mg m^{-2} was considered to be the recommended dosage for phase II studies, an additional four patients were enrolled at a dosage of 150 mg m^{-2}; one patient developed DLT, namely grade 4 neutropenia lasting for more than 5 days (Table 2). During the entire period of this study, G-CSF was never used to rescue patients.

Nonhaematological toxicity

The NK105 injection was generally uneventful and well tolerated in terms of nonhaematological toxicities (Table 2). Most of the toxicities were grade 1; none of the patients manifested grade 4 toxicity. A few patients developed a grade 1 elevation in AST or ALT, but these changes were transient. Pain or local toxicity in the area of the injection was not observed in any of the patients treated with NK105. No infusion-related reactions were observed; such reactions sometimes occur during liposomal drug administration. Patients were not premedicated with steroids or antihistamines. Only one patient at 180 mg m^{-2} developed grade 2 hypersensitivity. After the first course, the patient received premedication of hydrocortisone and did not develop such hypersensitivity after that. The other 18 patients did not experience any hypersensitivity during the study. Neuropathy occurred in a typical stocking/glove distribution and was manifested by numbness. Three patients at level 6 (150 mg m^{-2}) and three patients at level 7 (180 mg m^{-2}) experienced grade 1 neurotoxicity during 1 cycle. Of the four patients who received multicycle treatment more than five times, only three patients developed grade 2 neuropathy and the other patient developed grade 1 neuropathy. Even one patient who received 14 cycles of treatment experienced only grade 2 neuropathy.

Pharmacokinetics

The plasma concentrations of PTX after the intravenous infusion of NK105 were determined in each of the patients enrolled at a dose of 150 mg m^{-2} (Figure 2A). The C_{max} (Figure 2B) and AUC (Figure 2C) increased as the doses were escalated from 10 to 180 mg m^{-2}. The pharmacokinetic parameters are summarised in Table 3. The $t_{1/2Z}$ ranged from 7.0 to 13.2 h, and a slight tendency towards a dose-dependent extension of this parameter was observed. The CL_{tot} ranged from 280.9 to 880.4 ml h^{-1} m^{-2}, and the V_{ss} ranged from 3668.9 to 10 400.3 ml m^{-2}. Although these parameters were slightly reduced depending on the dose, linear pharmacokinetics was assumed to have been observed in the dose range from 10 to 180 mg m^{-2}. The AUC of NK105 at 150 mg m^{-2} (recommended phase II dose) was about 15-fold larger than that of conventional PTX at dose of 210 mg m^{-2} (conventional dose for a

Table 2 Haematological and nonhaematological toxicities (cycle 1 and all cycles)

	110–110 mg m^{-2} ($n=7$) grade				150 mg m^{-2} ($n=7$) grade				180 mg m^{-2} ($n=7$) grade			
	1	2	3	4	1	2	3	4	1	2	3	4
Cycle 1												
Leukopenia	2	0	2	0	1	5	1	0	1	1	3	0
Neutropenia	1	0	1	1	0	2	1	3[a]	0	0	3	2[b]
Thrombocytopenia	1	0	0	0	2	0	0	0	4	0	0	0
Hemoglobin	1	0	0	0	2	2	0	0	1	0	0	0
Neuropathy	0	0	0	0	3	0	0	0	3	0	0	0
Myalgia	1	0	0	0	3	0	0	0	2	1	0	0
Arthralgia	1	0	0	0	4	0	0	0	3	0	0	0
Hypersensitivity	0	0	0	0	0	0	0	0	0	1	0	0
Rash	1	0	0	0	1	3	0	0	4	0	0	0
Fatigue	1	0	0	0	5	0	0	0	4	0	0	0
Fever	2	0	0	0	2	0	0	0	1	0	1	0
Anorexia	0	0	0	0	3	0	0	0	1	0	0	0
Nausea	1	0	0	0	1	0	0	0	1	0	0	0
Stomatitis	0	0	0	0	1	0	0	0	1	0	0	0
Alopecia	3	0	—	—	5	0	—	—	5	0	—	—
All cycles												
Leukopenia	3	0	2	0	1	4	2	0	1	1	3	0
Neutropenia	1	0	1	1	1	1	1	4	0	0	3	2
Thrombocytopenia	1	0	0	0	3	0	0	0	4	0	0	0
Hemoglobin	1	0	0	0	1	5	0	0	1	0	0	0
Neuropathy	2	0	0	0	1	3	0	0	4	0	0	0
Myalgia	1	1	0	0	3	0	0	0	2	1	0	0
Arthralgia	2	0	0	0	4	0	0	0	3	0	0	0
Hypersensitivity	0	0	0	0	0	0	0	0	0	1	0	0
Rash	1	0	0	0	3	3	0	0	4	0	0	0
Fatigue	3	0	0	0	5	1	0	0	4	0	0	0
Fever	3	0	0	0	3	1	0	0	1	0	1	0
Anorexia	2	1	0	0	2	1	0	0	2	0	0	0
Nausea	1	0	0	0	1	0	0	0	2	0	0	0
Stomatitis	1	0	0	0	2	0	0	0	1	0	0	0
Alopecia	2	2	—	—	4	3	—	—	4	1	—	—

[a]One of three patients developed DLT, namely grade 4 neutropenia lasting for more than 5 days. [b]These two patients developed DLT, namely grade 4 neutropenia lasting for more than 5 days.

3-week regimen in Japanese patients) (Tamura *et al*, 1995). The V_{ss} and CL_{tot} of NK105 were significantly lower than those of conventional PTX.

The cumulative urinary excretion rates of PTX (0–73 h) after the administration of NK105 were 2.8–9.2%. These values were low, similar to those reported after the administration of conventional PTX (Tamura *et al*, 1995). The CL_r ranged from 11.7 to 66.4 ml h^{-1} m^{-3}, and was slightly decreased with the dose. Since the ratio of CL_r to CL_{tot} was 3–9%, CL_r hardly contributed to CL_{tot}.

Therapeutic response

Six patients (two gastric, two bile duct, one colon, and one pancreatic) were evaluated as having had a stable disease for longer than 4 weeks at the time of the study's completion. A partial response was seen in a patient with metastatic pancreatic cancer who had been treated at 150 mg m^{-2}, and in whom the size of the liver metastasis had decreased by more than 90%, compared to the baseline scan (Figure 3A). This patient had previously undergone treatment with gemcitabine. The antitumour response was maintained for nearly 1 year. In a patient with stomach cancer who was treated at 150 mg m^{-2}, about 40% reduction was observed in a peritoneal metastasis, but a liver metastasis remained stable (Figure 3B).

DISCUSSION

The observed toxicities of NK105 were similar to those expected for conventional PTX. The DLT was neutropenia. The recommended phase II dose using a 3-week schedule was determined to be 150 mg m^{-2}. This recommended dose of NK105 is less than that of conventional PTX (210 mg m^{-2}). Since the plasma AUC of the recommended dose of NK105 was 15- to 20-fold higher than that of the recommended dose of conventional PTX (210 mg m^{-2}), whether the so-called therapeutic window of NK105 is wider than that of conventional PTX should be determined in a future phases II or III trial, although the therapeutic window of NK105 appears to be wider than that of free PTX in mice experiments (Hamaguchi *et al*, 2005).

In general, haematological toxicity was mild and well managed in this trial. PTX is known to cause cumulative peripheral neuropathy resulting in the discontinuation of treatment with PTX. At a dose of 150 mg m^{-2}, three out of seven patients experienced only grade 1 neuropathy during the first cycle. Since the patients enrolled in this trial had almost intractable cancer, such as pancreatic or stomach, a relatively small number of patients received multiple cycles of treatment. Therefore, NK105-related neurotoxicity could not be evaluated in this study. However, three out of four patients who received more than five cycles of treatment experienced transient grade 2 peripheral neuropathy, and other patient developed transient grade 1 peripheral neuropathy. Future phase II trials may clarify whether NK105 is less toxic in terms of peripheral neuropathy when compared with conventional PTX, Abraxane, and other PTX compounds. Another characteristic adverse effect of PTX is hypersensitivity, which may be mainly caused by Cremophor EL. Since NK105 is not formulated in a Cremophor EL-containing solvent, we presumed that hypersensitivity would be diminished.